AGU PUBLICATIONS

Earth and Space Science

RESEARCH ARTICLE
10.1002/2016EA000196

Key Points:
- Annual planform changes mapped for large, dynamic meandering river from Landsat imagery
- RivMAP toolbox offers novel image processing-based techniques for analyzing channel masks
- Application to Ucayali River identifies sediment, cutoff, and climate controls on planform morphodynamics

Correspondence to:
J. Schwenk,
jonschwenk@gmail.com

Citation:
Schwenk, J., A. Khandelwal, M. Fratkin, V. Kumar, and E. Foufoula-Georgiou (2017), High spatiotemporal resolution of river planform dynamics from Landsat: The RivMAP toolbox and results from the Ucayali River, *Earth and Space Science*, *4*, 46–75, doi:10.1002/2016EA000196.

Received 16 JUL 2016
Accepted 7 NOV 2016
Accepted article online 10 NOV 2016
Published online 1 FEB 2017

©2016. The Authors.
This is an open access article under the terms of the Creative Commons Attribution-NonCommercial-NoDerivs License, which permits use and distribution in any medium, provided the original work is properly cited, the use is non-commercial and no modifications or adaptations are made.

High spatiotemporal resolution of river planform dynamics from Landsat: The RivMAP toolbox and results from the Ucayali River

Jon Schwenk[1], Ankush Khandelwal[2], Mulu Fratkin[1], Vipin Kumar[2], and Efi Foufoula-Georgiou[1,3]

[1]Department of Civil, Environmental and Geo- Engineering and Saint Anthony Falls Laboratory, University of Minnesota, Twin Cities, Twin Cities, Minneapolis, USA, [2]Department of Computer Science and Engineering, University of Minnesota, Twin Cities, Twin Cities, Minneapolis, USA, [3]Department of Civil and Environmental Engineering, University of California, Irvine, California, USA

Abstract Quantifying planform changes of large and actively migrating rivers such as those in the tropical Amazon at multidecadal time scales, over large spatial domains, and with high spatiotemporal frequency is essential for advancing river morphodynamic theory, identifying controls on migration, and understanding the roles of climate and human influences on planform adjustments. This paper addresses the challenges of quantifying river planform changes from annual channel masks derived from Landsat imagery and introduces a set of efficient methods to map and measure changes in channel widths, the locations and rates of migration, accretion and erosion, and the space-time characteristics of cutoff dynamics. The techniques are assembled in a comprehensive MATLAB toolbox called RivMAP (River Morphodynamics from Analysis of Planforms), which is applied to over 1500 km of the actively migrating and predominately meandering Ucayali River in Peru from 1985 to 2015. We find multiscale spatial and temporal variability around multidecadal trends in migration rates, erosion and accretion, and channel widths revealing a river dynamically adjusting to sediment and water fluxes. Confounding factors controlling planform morphodynamics including local inputs of sediment, cutoffs, and climate are parsed through the high temporal analysis.

1. Introduction

Efforts to map and measure migrating meanders have resulted in fruitful insights into the dynamics of these fascinating fluvial forms. However, the difficulty of observing multidecadal river migrations at high temporal and spatial resolutions has hampered efforts to fully resolve natural planform dynamics [*Hooke*, 2003]. Observations made over longer periods (decades to centuries) are often compiled from various sources such as historic maps, surveys, and aerial photographs that do not capture planform changes [*Hooke and Redmond*, 1989; *Harmar and Clifford*, 2006; *Yao et al*., 2012] due to nonstationary flow regimes [*Bradley and Smith*, 1984; *Kiss and Blanka*, 2012], individual floods [*Hickin and Sichingabula*, 1989; *Nagata et al*., 2014], cutoffs [*Hooke*, 2004; *Zinger et al*., 2011; *Martha et al*., 2014], or human activities [*Asner et al*., 2013; *Midha and Mathur*, 2014; *Słowik*, 2015; *Rhoads et al*., 2016]. On the other hand, studies that resolve detailed migration dynamics at event-scale frequencies from aerial photographs are often constrained to significantly shorter durations than the inception-to-cutoff time of a typical meander bend [e.g., *Bertoldi et al*., 2010]. Highly temporally resolved meander dynamics have been estimated over longer durations from scroll bars [*Rodnight et al*., 2005], point bar surfaces [*Hickin and Nanson*, 1975], and tree rings [*Handy*, 1972], but such studies are not spatially continuous over distances larger than a few meander bends. Many researchers have turned to numerical modeling to simulate river planform and floodplain development over long durations and large spatial domains with high temporal frequency [*Howard*, 1996; *Sun et al*., 1996; *Stolum*, 1998; *Perucca et al*., 2006; *Xu et al*., 2011; *Bradley and Tucker*, 2013; *Schwenk et al*., 2015b]. However, validation of such long time models has received less attention, due largely to the limited availability of observations [*Howard*, 1996].

Satellite imagery offers the potential to map spatially continuous planform changes over large domains and with high temporal resolution. The thematic mapper sensors aboard Landsat satellites have collected worldwide imagery at 30 m resolution at least every 16 days since the launch of Landsat 5 (L5) in 1984. In terms of observing natural fluvial planform change, 30 m Landsat data overcome the obstacles of poor temporal

resolution and limited spatial coverage, but their 32 year record is significantly shorter than the inception-to-cutoff time scale of most meandering rivers. Nevertheless, a growing number of studies have leveraged Landsat imagery to map and measure planform changes of major rivers [e.g., *Yang et al*., 1999; *Baki and Gan*, 2012; *Gupta et al*., 2013]. Rivers flowing through the tropical Amazon region have been of particular interest [*Kalliola et al*., 1992; *Constantine et al*., 2014; *Schwendel et al*., 2015] partly due to their rapidly changing planforms. For example, full lifecycles (i.e., inception to cutoff) [*Schwenk et al*., 2015b] for a number of smaller meander bends in the Amazon were captured within the growing 32 year window of Landsat imagery. Most studies of river changes resolved the planforms at time intervals longer than 2 years, although *Frias et al*. [2015] analyzed two anabranching bends using annual time steps, as did *Gautier et al*. [2007] for a reach of the Rio Beni over a 5 year period.

This work represents an effort to map and measure annual bankfull planform dynamics from Landsat imagery for over 1500 km of the Ucayali River in Peru from 1985 to 2015 in order to advance our quantitative understanding of river morphodynamics, as a function of climatic and human actions. The Ucayali was chosen for its rapid dynamics which resulted in 42 cutoffs in a 30 year period [see also *Schwenk*, 2016]. Toward this goal, a suite of modules written in MATLAB was developed to quantify channel planform changes from binary channel masks and compiled into a MATLAB toolbox called RivMAP: River Morphodynamics from Analysis of Planforms. Figure 1 presents a schematic overview of RivMAP in terms of the steps involved and products produced. A variety of toolsets are already available for determining planform channel characteristics from remotely sensed imagery and/or planform maps. The recent paper of *Rowland et al*. [2016] presents a detailed comparison of nine such tools; we therefore present the metaproperties of five software packages designed to assess river planform characteristics and/or quantify planform change (Table 1). Of these, SCREAM [*Rowland et al*., 2016] and RivMAP offer the most comprehensive set of analysis tools, with the primary difference between SCREAM and RivMAP being the former's bank-centric approach versus the latter's centerline-centric. RivMAP's development was motivated by studies of meander migration that consider centerline evolution [see *Güneralp et al*., 2012; *Hooke*, 2013], while SCREAM was primarily developed to address questions of bank dynamics.

This paper is organized as follows. Section 2 describes the study reach of the Ucayali River. Section 3 details the process of using Landsat data to create annual, bankfull-resolving channel masks. Section 4 introduces RivMAP and describes its functions for quantifying planform characteristics and changes. Section 5 shows the multiscale spatial and temporal variability of planform changes along the Ucayali River quantified via RivMAP and presents an uncertainty analysis. Section 6 discusses the insights gained from quantifying planform changes annually, and the paper concludes with an overview of the analysis and potential applications of RivMAP toward developing a mechanistic understanding of river morphodynamics.

2. Study Area: The Ucayali River in Peru

The Ucayali River flows south-to-north through Peruvian rainforest along the southeastern base of the Andes Mountains before joining the Marañon River to become the Amazon River about 100 km south of Iquitos, Peru. Although the Ucayali begins near Cusco, Peru in the Andes Mountains, its remarkably active migration begins near the city of Atalaya at its confluence with the Tambo River. From its headwaters in the Arequipa region of Peru to its confluence with the Marañon River, the Ucayali stretches approximately 2670 km, but this study focuses only on the final 1500 km between the confluences with the Tambo and Marañon Rivers (Figure 2). The study reach of the Ucayali exhibits some braiding and anabranching but features a predominately single-thread, meandering planform with many bends that contain secondary chute channels.

The Ucayali River is extraordinarily dynamic, featuring abundant cutoffs and point bar developments. Oxbow lakes and scroll bars pepper its floodplain. An annual average migration rate of 36 m/yr was recently reported [*Constantine et al*., 2014], but migration rates exceeding 750 m/yr were observed locally along some bends. The Ucayali's extraordinary activity is driven, in part, by large sediment loads supplied by four major tributaries draining the westerly Andes Mountains (56% of its catchment is Andean) and sediment and flow contributions from nearly a dozen smaller tributaries from the easterly Amazon rainforest. Our study found bankfull widths ranging from 400 to over 1500 m with an average of about 825 m, and the average depth was reported as 10 m though scour holes are sometimes 10 m deeper than the average bed elevation [*Ettmer and Alvarado-Ancieta*, 2010]. Mean annual flows at the confluence with the Amazon River have been

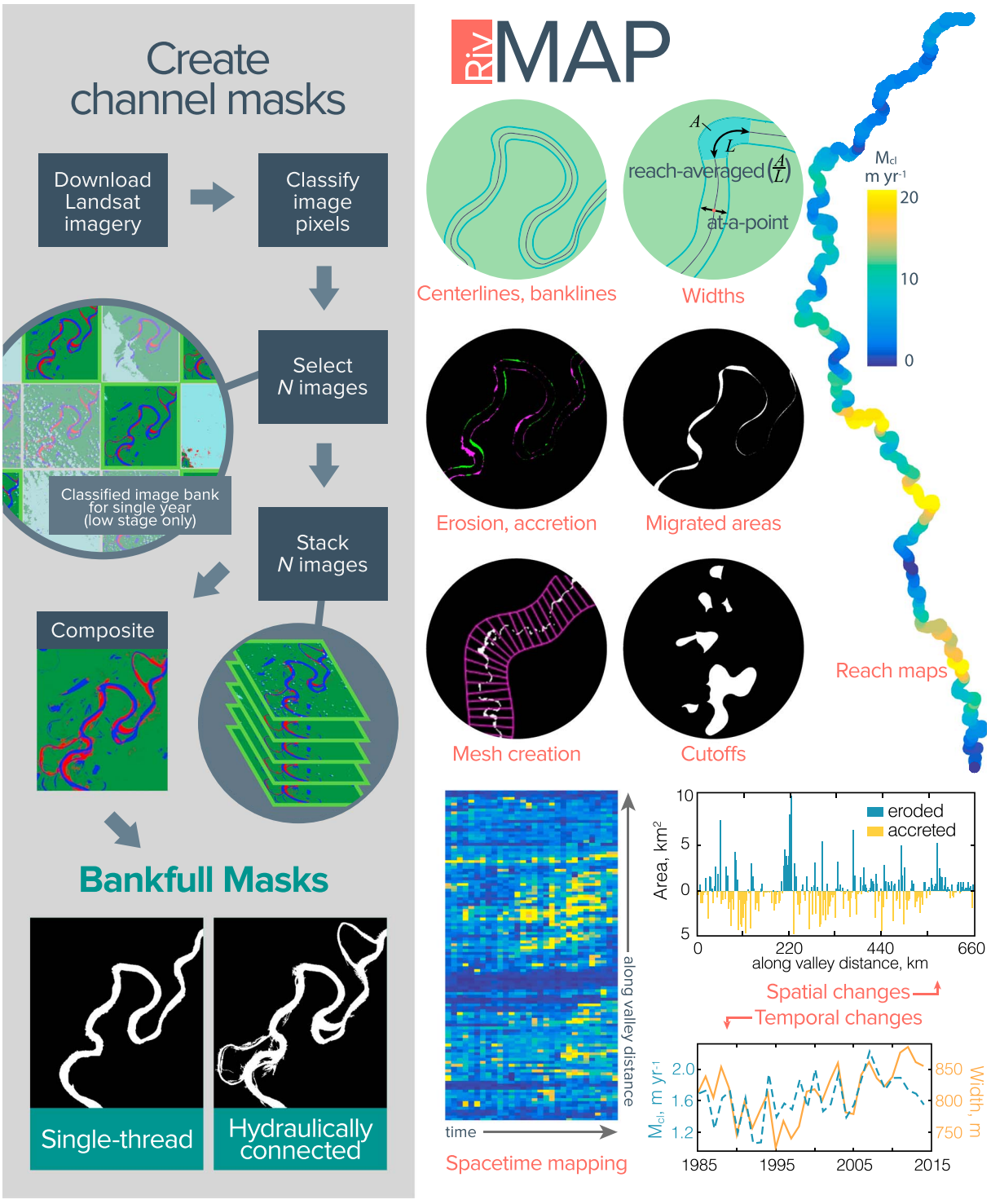

Figure 1. (left) Our procedure to create annual, bankfull-resolving channel masks is illustrated. The classified images are from the Ucayali River. (right) Examples of RivMAP's tools for quantifying planform characteristics and dynamics are illustrated. The spacetime and reach maps are shown for migration rates (M_{cl}), but any metric of planform change may be considered, including width, erosion, accretion, sediment area, or sinuosity.

Table 1. Metaproperties of Software Packages to Measure Planform Characteristics and Morphodynamics[a]

Package	Platform	GUI	Input	Planform Dynamics	Channel Type(s)	Primary Motivation
Channel Migration Toolbox[b]	ArcGIS	yes	Centerlines or banklines	yes	ST	Effect of lateral channel migration rates on floodplain ecology
RivWidth[c]	IDL	no	Channel masks	no	ST, MT	Automated width calculations over large domains
ChanGeom[d]	MATLAB	no	Channel masks	no	ST	Tectonic effects on channel planform geometry
SCREAM[e]	IDL	n/a[e]	Channel masks	yes	ST, MT	Bank dynamics esp. in polar regions
RivMAP	MATLAB	no	Channel masks	yes	ST, MT	Meander planform morphodynamics of highly active rivers

[a]Channel types include single threaded (ST) or multithreaded (MT).
[b]*Legg et al.* [2014] but was built around the Planform Statistics Toolbox by Wes Lauer [*Lauer*, 2006]. For an open-source GRASS GIS-based toolset with similar capabilities, see *Clerici and Perego* [2016].
[c]*Pavelsky and Smith* [2008] and *Allen and Pavelsky* [2015].
[d]*Fisher et al.* [2013].
[e]*Rowland et al.* [2016].
[f]SCREAM requires no user intervention (i.e., selection of parameters or thresholds) beyond input masks.

reported to range from around 9500 m^3/s [*Gibbs*, 1967] to 13,500 m^3/s [*Espinoza Villar et al.*, 2009], but discharge is cyclic with a strong seasonal dependence [*Lavado Casimiro et al.*, 2013]. Flow and sediment ($D_{50} = 0.25$ mm) are transported along slopes on the order of 10^{-4} [*Ettmer and Alvarado-Ancieta*, 2010]. The river is relatively unimpacted by anthropogenic activity, although at least one major cutoff event was unintentionally initiated by locals near the Masisea community [*Abizaid*, 2005; *Coomes et al.*, 2009]. The Ucayali River is vital to the livelihoods of nearly 500 local communities [*Webster et al.*, 2016], providing economic and transportation benefits to millions of Peruvians [*Coomes et al.*, 2009].

For this study, the Ucayali River was divided into four subregions (R3–R6, Figure 2c) in order to reduce the computational demand of downloading and processing imagery. Each subregion's boundaries were drawn to intersect the river at reaches that underwent relatively minimal planform changes as observed from Google Earth Engine. Eight Landsat scenes contributed imagery to resolve the river within each subregion. The Ucayali contains a major avulsion in R3 (Figure 2, R3) where the southern reach is approximately twice the width of its northern counterpart. Both avulsions were retained in the analysis, although reach-wide analyses only include the wider southern branch.

3. Annual Bankfull Channel Masks From Landsat Imagery

Continuous, worldwide satellite imagery at 30 m resolution was first collected by NASA's Landsat 5 (L5) beginning in 1984, providing complete satellite imagery of Earth every 16 days. We downloaded images of the Ucayali River spanning 1985–2015 acquired by L5 and Landsat 7 (L7) satellites using the Google Earth Engine. Most images of the Ucayali were at least partially obscured by clouds, and in 2003 the scan line corrector (SLC) aboard L7 failed, resulting in stripes of missing data across all its succeeding scenes (see boxes 1–4 in Figure 4). These complications prevented analysis of the entire study reach at subannual time scales. Instead, we distilled more than 135,000 Landsat images into annual, bankfull-resolving channel masks. The following sections describe the processes of classifying Landsat images, combining them into annual composites and creating channel masks with further details of the procedures given in Appendix A and Appendix B.

3.1. Classifying Landsat Imagery

Each pixel of each image was classified as sediment, water, land, or cloud using support vector machine (SVM) classification models [*Pal and Mather*, 2005; *Bazi and Melgani*, 2006; *Foody and Mathur*, 2006]. An M-dimensional phase space was constructed by assigning each spectral Landsat band an axis, where $M = 7$ and 8 for L5 and L7, respectively. The phase space was populated by training data containing pixels of known class, and hyperplanes were constructed that delineated class regions. The classification of an unknown pixel was determined according to which class region it lied within the phase space. A total of eight SVM models were constructed, corresponding to an L5 and L7 model for each of the four R subregions (Figure 2). For each pixel, the corresponding SVM model searched for a positive identification of a single class. If none were

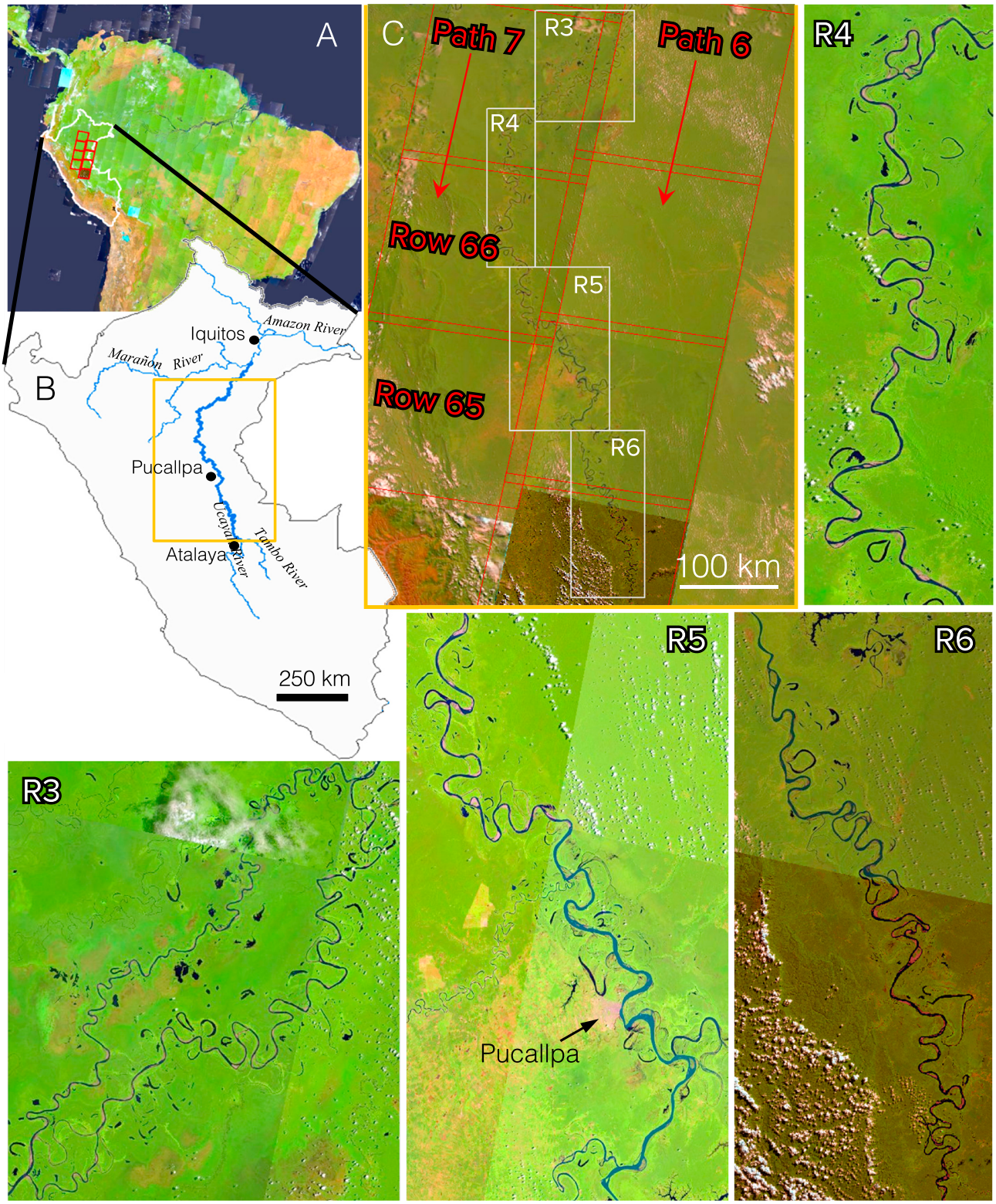

Figure 2. (a) The Landsat scenes covering the study area are shown by the eight red boxes. (b) The extents of the study reach within Peru are delimited by an orange box. (c) A zoom view of the extents with the Landsat scenes (red) and the four subregions (R3–R6) overlain (white boxes). The eight Landsat scenes intersecting the R boundary boxes range from Path 7, Row 64 (top left) to Path 6, Row 67 (bottom right). Each of the R bounding boxes is shown in more detail; the lower portion of the Ucayali's avulsion in the R3 box is considered the main channel for the analysis. Imagery is the latest available from the Landsat 8 Views collection spanning 2015–2016.

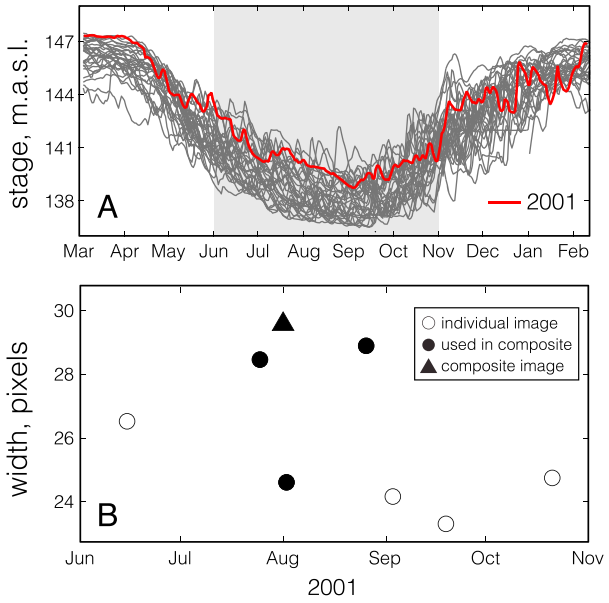

Figure 3. (a) Each gray line is a year of stage recordings of the Ucayali River at Pucallpa, Peru, from 1981 to 2015. The red line shows stages in 2001. The shaded region delineates the period over which individual Landsat images were used for compositing. (b) Average widths of the Ucayali River within R4 (see Figure 2) are shown for individual Landsat images in 2001 (open and filled circles), while the filled circles show the three images used to create the composite. The width of the composite image for 2001 (filled triangle) is plotted at the nominal date of 1 August.

found, the next class was checked until either the pixel was successfully classified or could not be described by any of the classifications. The sediment class was checked first, followed by water, land, and finally cloud.

Classification uncertainty was greatest for pixels representing partially inundated or vegetated bars, which often carry a "fuzzy" spectral signature [*Allen and Pavelsky*, 2015]. The "true" class of a pixel cannot be reliably assessed without field verification. The sediment pixels included in the training set were chosen from areas without this ambiguity, and our classifier was thus conservative in sediment-pixel identifications. In some cases the spectral similarity of clouds and water resulted in the classification of clouds as water, which if connected to the main channel were manually removed.

3.2. Compositing Images

For each year, selected individual classified images were "smashed" together to make a single composite image. Annual composites are required to overcome some difficulties inherent in using Landsat imagery. Landsat scenes within the same path are observed on the same day, but scenes from adjacent paths are collected at a minimum of eight days later. Thus, where the river crosses Landsat paths (e.g., from path 6 to 7 for the Ucayali), a complete image of the river will not be available for the same date, and a composite is necessary. Composites also allow information to be included from scenes that are partially obscured by cloud cover or SLC-off stripes and reduce classifier uncertainty near boundaries.

Composite images have additional benefits beyond overcoming data shortcomings; they maximally resolve exposed in-channel sediment (bar morphologies) and provide consistent estimates of the bankfull channel planform. In order to compare planforms interannually, the delineation of the river planform boundaries should be independent of river stage. In other words, an estimate of the bankfull channel planform [*Williams*, 1978] is required. Conceptually, the bankfull stage represents the water level at which flow begins to spill from the channel onto the floodplain. Field evidence of bankfull stage includes breaks in bank slope, changes in near-bank vegetation, transitions in soil type, and tops of bars [*Harrelson et al.*, 1994]. In the absence of detailed field measurements across the large space and time domains of this study, we defined the bankfull channel planform area by the primary channel (water pixels) plus connected exposed bars (sediment pixels).

Images composited through time will also integrate planform changes into the final composite. For example, if a series of images through which the river undergoes substantial migration is used to create a composite, the composite image would contain an artificially wider planform. In order to ensure a near-stationary channel across individual images, only those from periods of low discharges when lower shear stresses prevent substantial migration were selected for use. Flow in many tropical rivers is highly seasonal [*Latrubesse et al.*, 2005]; in the Ucayali, flows tend to be lower from June to October and larger from January to April (Figure 3a). These drier months are also conveniently the least cloudy and therefore provide the clearest views of the river. Very few unobscured Landsat images were available of the river at flood stage. Within R4, only two such images existed over the 1985–2015 period. A comparison between the bankfull-stage image and composite image confirmed that the composite planform agreed with the high-stage (bankfull) planform (Figure 4).

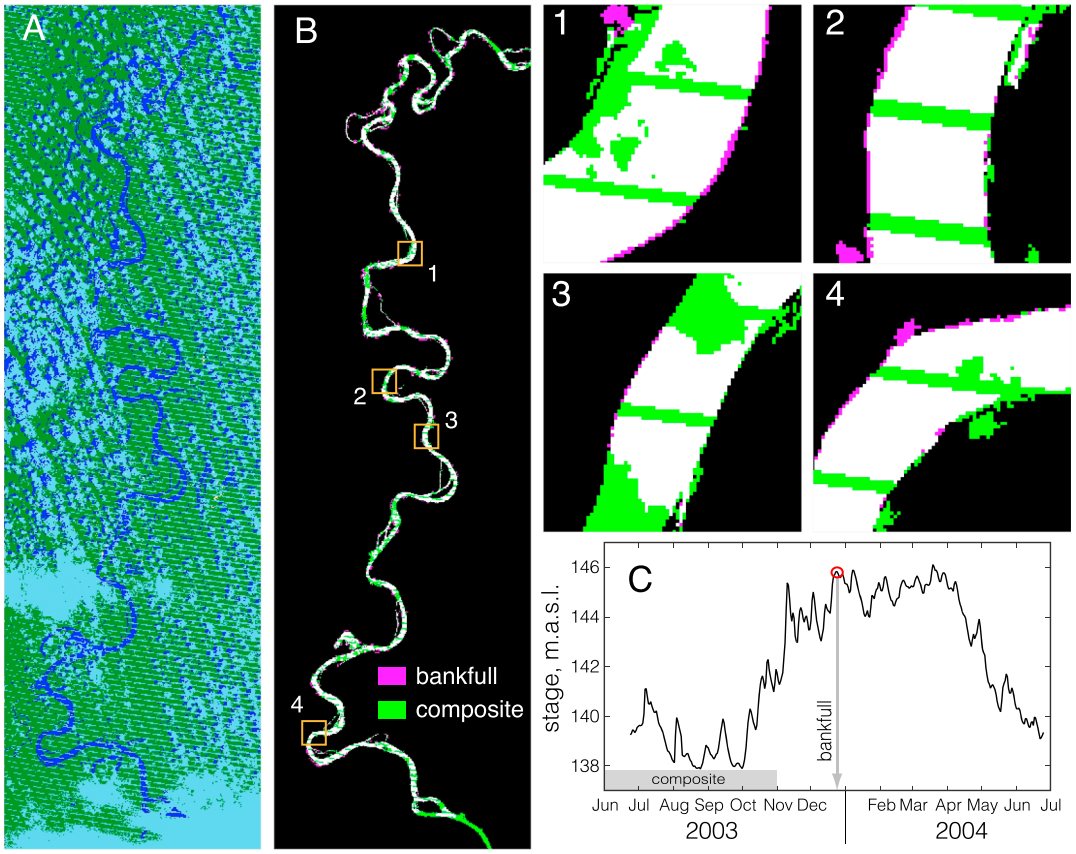

Figure 4. The river's planform at flood stage (bankfull) is compared with its planform from the composite image of the same water year. (a) The classified Landsat image from 24 December 2004 (R4) is shown. The river is at flood stage; note the absence of exposed sediment (red pixels). (b) The bankfull channel mask is superimposed with the composite. Magenta indicates the presence of only bankfull channel, green shows the presence of only the composite image, and white corresponds to the presence of both. Four reaches displayed in more detail (1–4) show that the differences between the bankfull image and composite occur predominately at outer banks, implying that migration is responsible for the discrepancies rather than an incomplete composite. The nearly complete overlap of the flood-stage mask and composite demonstrates that the composite reasonably captures the bankfull channel planform. (c) River stage is shown from 2004 to 2005 with the stage at the time of the bankfull image in Figure 4a denoted by a red circle. The grey box spans the period over which images were drawn from for compositing, while the grey arrow points to the day of the bankfull image.

Through the compositing process, gaps and misclassifications of sediment from individual images are filled in by sediment identified in others. Average width computed from seven Landsat images (R4) within a single year where an unobscured view of the river was available demonstrates the variability of widths measured from individual classified Landsat images alone (Figure 3b). Widths obtained from individual images ranged from 23 to 28.5 pixels, while the composite image necessarily resulted in a greater average width (29 pixels) than any of the individual images. The greater width of the composite image reflects sediment contributions from the individual images wherein misclassified or unknown pixels in the individual images are filled with information from the other images.

Details of the compositing algorithm are given in Appendix A, and an example is shown in Figures 5a–5d. The compositing process revealed errors in georectification of some Landsat images, where misgeorectified images created an obvious "double image" (Figures 5e and 5f). A total of 20 scenes from the June to November window in 1985–2015 across all R boxes were found to be misaligned. These images were detected by examining each composite for double images and removing the misgeorectified image from the stack which was subsequently recomposited. In 2016, the USGS announced a reprocessing of all Landsat imagery to correct these and other geolocation errors, but the corrected Landsat products were not available at the time of this study.

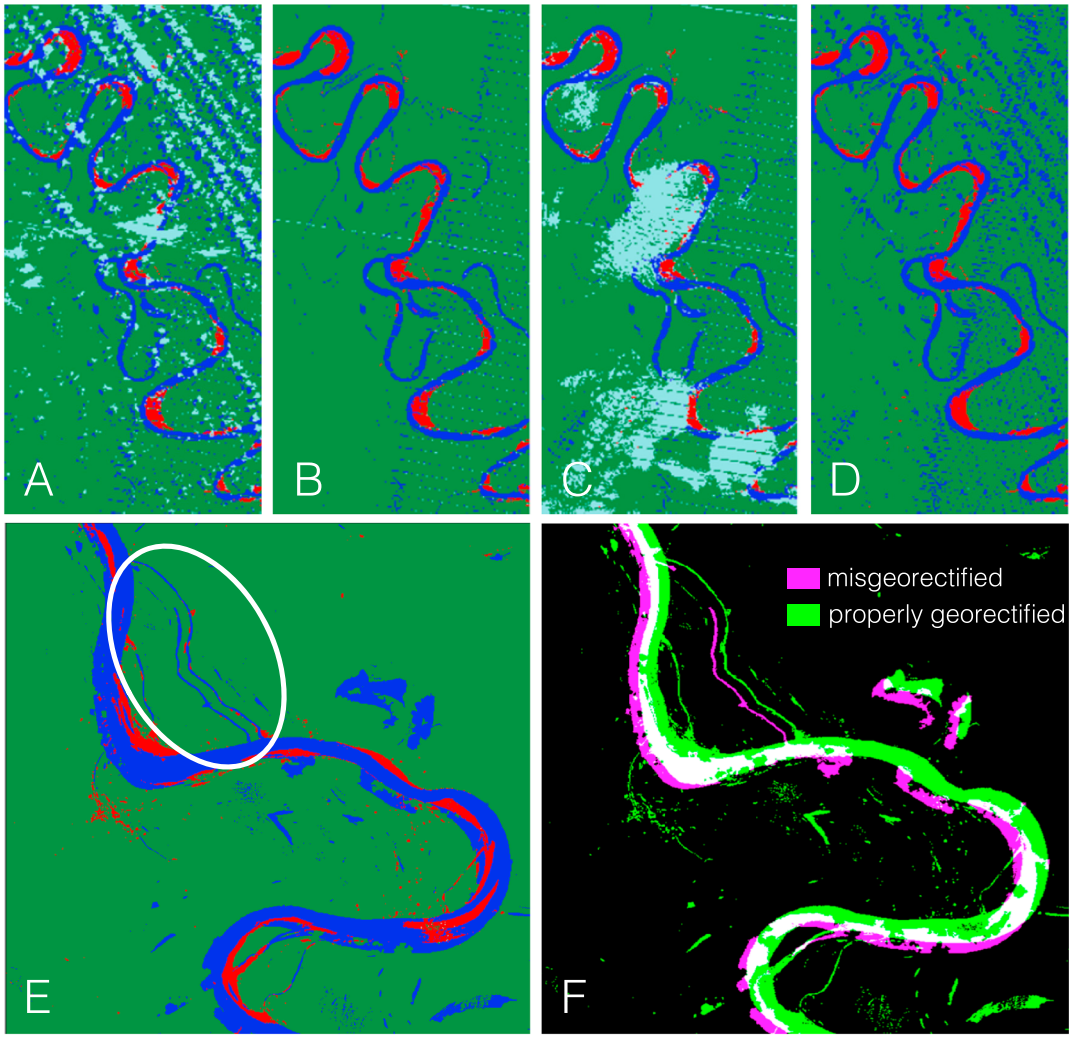

Figure 5. (a–c) Three classified Landsat images from different dates are used to create a (d) composite image. Blue is water, red is sediment, and light blue is cloud. The portions of river obscured by clouds in Figures 5a and 5c and the scan line corrector-off lines in Figures 5b and 5c are resolved in the final composite by information from the other images. Undesirable cloud shadows in Figure 5a classified as water are carried through to the composite. (e) An example of a composite created with an incorrectly georectified Landsat scene. The improper alignment was readily observed by the double chute channel (circled), and the image was removed from stack. (f) The two binary masks of the Landsat images used to create the composite are superimposed. This scene is from R4, 1989, and the individual images were taken 96 days apart.

3.3. Creating Channel Masks From Composite Images

Each annual composite image was manually cleaned by removing all connected components that were not hydraulically connected to the river (i.e., tributaries, cities, and cutoff remnants). Additionally, noise in the composite images from errant classifications (e.g., clouds identified as water) was removed wherever it intersected the channel body. Hydraulically connected binary channel masks were created for cleaned composites from the largest set of all connected water and sediment pixels. Planform statistics including migration rate, width, radius of curvature, and channel direction require a well-defined centerline. The Ucayali River's abundant chute channels, avulsions, connections to oxbow lakes, tributaries, and riverside cities required manual disconnection from the main channel body before a centerline could be identified. This cleaning process resulted in a binary mask mapping the full, hydraulically connected extents of the river and a binary mask representing only the primary channel for each annual composite. Details of manual cleaning are given in Appendix B.

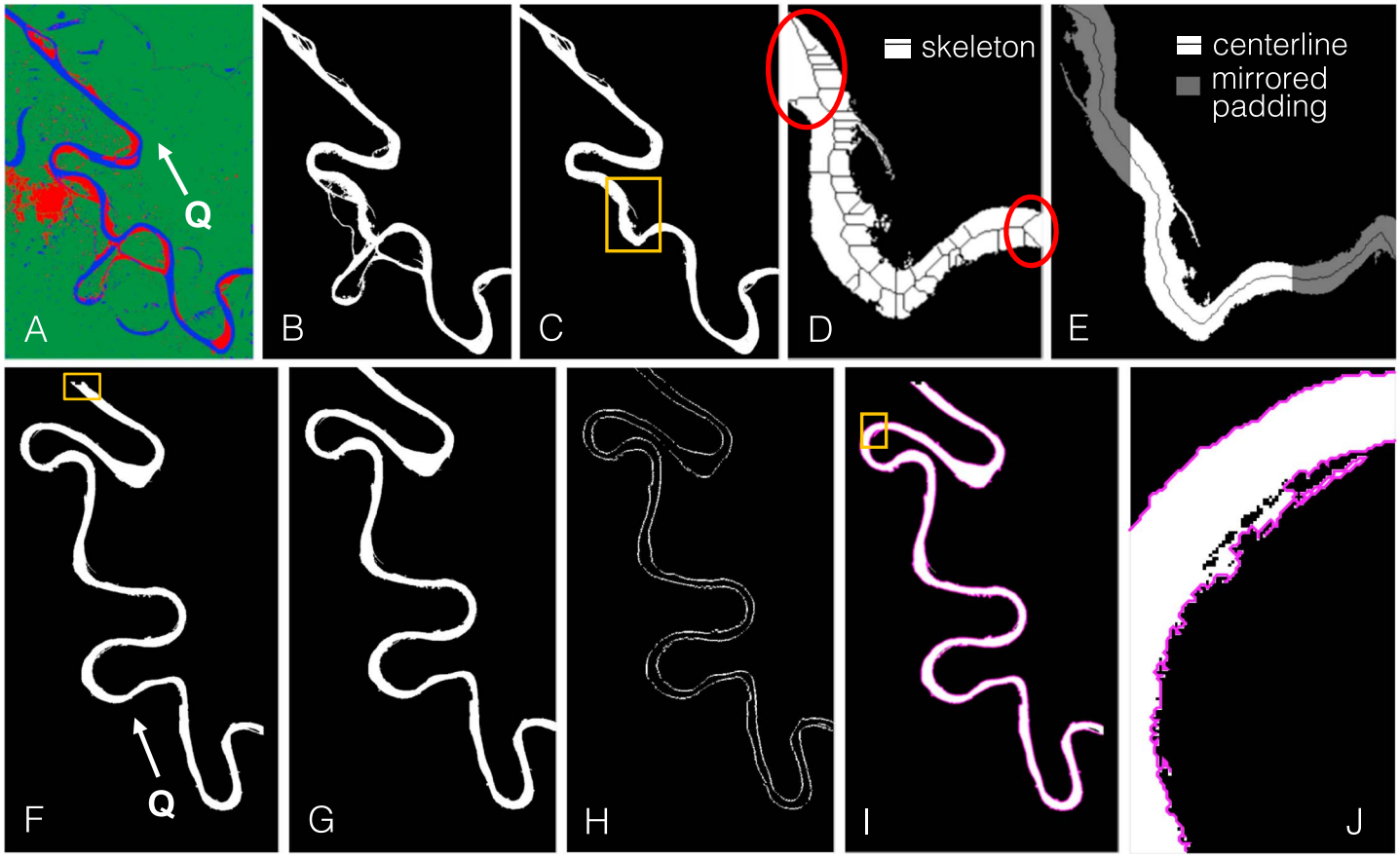

Figure 6. The steps for obtaining a (a–e) centerline and (f–j) banklines from a composite image are illustrated. A composite image is shown in Figure 6a from R5, 1989. The red patch is the city of Pucallpa, Peru. In Figure 6b the cleaned, hydraulically connected channel mask is shown, and its single-thread counterpart is shown in Figure 6c. The orange box denotes the extents of the image in Figure 6d. In Figure 6d, the skeleton of the channel mask is shown. The problematic ends of the skeleton are circled. The padding technique for resolving the ends of the centerline is illustrated in Figure 6e along with the skeleton endpoints and final centerline for the channel mask. The steps for extracting banklines from a channel mask are illustrated in the Figures 6f–6j. A binary channel mask from R5, 2007, is shown in Figure 6f with a notch artificially removed from the downstream end (orange box). The image after cropping is shown in Figure 6g and its perimeter in Figure 6h. The extracted banks are shown in Figure 6i, and a zoom view in Figure 6j shows how the banklines follow the edge of the rough channel mask.

4. River Morphodynamics From Analysis of Planforms (RivMAP)

RivMAP provides tools for quantifying static planform geometries from binary channel masks including centerline and bankline extractions, widths, lengths, angles, and curvatures. It also provides functions to measure changes in time, including centerline and bankline migrated areas, areas of erosion and accretion, and cutoff identification, and creates reference grids for mapping these changes. No graphical user interface (GUI) is currently offered, but functions are written intuitively and well commented for ease of customization and application to specific research questions. RivMAP relies primarily on MATLAB's built-in image-processing morphological operations, such as erosion, dilation, hole-filling, skeletonization, and distance transforms, to efficiently compute relevant outputs from channel masks. While most of the tools included in RivMAP may be also found in other packages, some of its tools offer innovative solutions to image-based processing problems. The construction of a grid for space-time mapping (section 4.5) a novel method for mapping high temporal resolution planform changes. RivMAP also contains a function to stitch together georeferenced imagery so that results may be recombined for postprocessing. The following sections describe the technical details of RivMAP functions. A link to download RivMAP and a demo with data from the R6 subregion of the Ucayali River are provided in the acknowledgements.

4.1. Centerlines and Banklines From Channel Mask

The RivMAP tool for obtaining a centerline from an image mask (*centerline_from_mask*) requires only two inputs: a channel mask and a two-character variable (exit_sides) that denotes the sides which the channel

enters (upstream) and leaves (downstream) the image. (RivMAP does not currently support cases where the river enters and leaves the image on the same side.) First, holes in the input mask are filled, and any areas of the mask not connected to the main channel are removed. The mask is then skeletonized by evenly eroding its boundaries without breaking its connectivity [*Lam et al*., 1992; *Pavelsky and Smith*, 2008; *Kieler et al*., 2009; *Fisher et al*., 2013]. Skeletonization resolves the centerline well but poses two problems. First, the skeleton at the ends of the channel mask no longer traces the centerline, as it must intersect the corners of the object (channel mask) being skeletonized (Figure 6d). This is overcome by padding the channel mask image with mirrored versions of itself, providing a channel with smooth transitions beyond the boundaries of original mask. The centerline is obtained from the padded image and then cropped to remove the boundary effect of skeletonization. The second problem of skeletonization is the presence of unwanted spurs that must be removed (Figure 6d). Rather than removing spurs individually [e.g., *Fisher et al*., 2013], the centerline is found as the shortest path along the skeleton between its endpoints. The coordinates of the shortest path are arranged from upstream to downstream and returned as a two-column vector. The centerline is resolved at single-pixel resolution, so centerline node spacing depends on the resolution of the input mask. Centerlines may be computed for both single-threaded and multithreaded channels, but for the latter the centerline of the holes-filled channel mask will be returned.

Banklines are extracted from a binary channel mask by taking advantage of MATLAB's efficient image processing tools. The *banklines_from_mask* function requires inputs of a channel mask and its exit sides; if the input mask contains a multithreaded channel, only the outermost banklines will be returned. The mask image is first cropped such that the ends of the river intersect the edge of the image, and any holes within the mask that border the image boundary are filled (Figures 6f and 6g). The perimeter of this image is found and separated into left and right banks by removing all pixels at the image boundaries except the bankline pixels (two for each exit side). Bankline coordinates are evaluated to determine the left and right banks (looking downstream) and arranged in an upstream-to-downstream order.

4.2. River Widths

RivMAP's *width_from_mask* routine computes the average channel width at specified intervals along the channel centerline and returns the wetted width for both single-threaded and multithreaded channels. The *width_from_mask* routine requires inputs of a channel mask, its centerline, and the desired interval along the centerline to compute widths. The centerline is parameterized by the streamwise distance computed between successive (x_i,y_i) centerline points:

$$ds_i = \sqrt{(x_{i+1} - x_i)^2 + (y_{i+1} - y_i)^2} \tag{1}$$

The reach-average width of the entire channel mask is then computed for use in parametrizing centerline smoothing and buffer sizing:

$$W_{ra} = \frac{P}{\Sigma ds_i} \tag{2}$$

where P is the number of pixels in the holes-filled channel mask and the summation of ds_i is over all centerline nodes in the channel mask [*Smith et al*., 1996; *Rowland et al*., 2016]. Centerline coordinates are smoothed to provide a continuous, stable estimate of the centerline direction at each node computed as

$$\theta_i = \arctan\left(\frac{y_{i+1} - y_i}{x_{i+1} - x_i}\right). \tag{3}$$

The centerline is broken into J equally spaced segments of user-selected length, and a buffer polygon is created for each jth segment by first constructing perpendicular vectors at the first and last nodes of the segment. The perpendicular vectors are connected by polylines defined from the centerline nodes within segment j for the left and right banks:

$$\begin{aligned}\left(x_{lb,i}, y_{lb,i}\right) &= (x_i - (\sin(\pi - \theta_i))2W_{ra}, y_i - (\cos(\pi - \theta_i))2W_{ra}) \\ \left(x_{rb,i}, y_{rb,i}\right) &= (x_i + (\sin(\pi - \theta_i))2W_{ra}, y_i + (\cos(\pi - \theta_i))2W_{ra})\end{aligned} \tag{4}$$

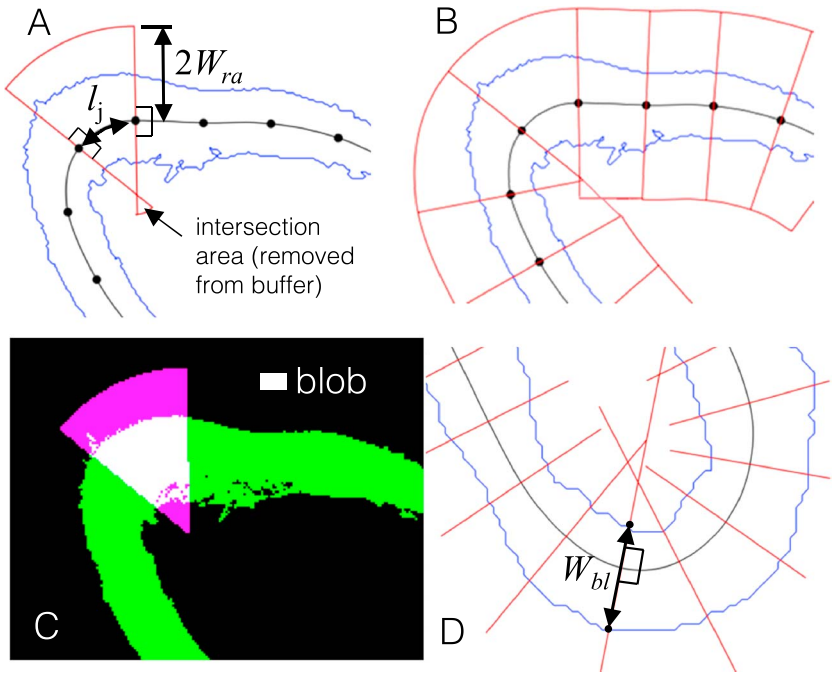

Figure 7. The procedures for computing width are illustrated. (a) Average width (W_{avg}) for a segment of river is computed by first drawing buffer boundaries. The smooth centerline is shown in black, and the buffer spacings (shown here as 30 pixels) are shown by black dots. (b) Buffer polygons are shown for each spacing. (c) A buffer is overlain on the channel mask. The white area is the blob created by the intersection of the buffer and mask images. The average channel width of the section is the number of blob pixels divided by l_j. (d) A diagram illustrating the computation of channel width from banklines. Channel banks are in blue and the smoothed centerline in black. Perpendicular vectors are shown for every tenth pixel in red.

This scheme creates buffer polygons that follow the channel planform direction rather than rectangular buffers which can produce excessive unwanted overlap, especially along sharp bends. In regions of high centerline curvature, the perpendicular vectors at the beginning and ending of segment *j* may intersect; in these cases the buffer is truncated at their intersection (Figure 7a). It is possible but rare for this intersection to occur within the channel at wide reaches of large curvature leading to RivMAP's halting. The buffer polygon is converted to a binary image of the same size as the input mask, and the intersection of the buffer mask with the channel mask returns the number of channel mask pixels within the *j*th buffer (P_j). The centerline length within each *j*th buffer is found by

$$l_j = \sum_{i(j)}^{i(j+1)} ds_i \tag{5}$$

where $i(j)$ refers to the *i*th centerline node at the beginning of segment *j*. The width of segment *j* is finally computed as

$$W_{\mathrm{avg},j} = \frac{P_j}{l_j} \tag{6}$$

where P_j is the number of pixels in segment *j*. This approach for computing width is susceptible to errors associated with pixel-based line lengths [*da Paz et al*., 2008]. *Rowland et al*. [2016] found a consistent error of 6% between average channel widths and pointwise measurements but were able to reduce this error to 3% by applying corrections proposed by *Butt and Maragos* [1998].

Buffers are conservative in the sense that each pixel in the channel mask belongs uniquely to a buffer, i.e., no pixel is double counted and no pixel is uncounted. Typically, the overlap between the buffer and the channel mask contains only one region of connected area called a "blob" (see Figure 7c). However, in some cases, particularly where the river doubles back on itself, the buffer might also overlap a portion of the doubled back reach resulting in multiple blobs. Unwanted blobs are detected by computing the distance from the centroid of each blob to the midpoint of the centerline between the beginning and ending nodes

of segment *j*. If this distance is greater than $1.5\overline{l_j}$ the blob is removed, where the overbar denotes the mean over all *j* segments.

Channel widths between banklines at each centerline node may be computed from banklines with the *width_from_banklines* function, which requires inputs of the left and right banks, centerline, and a nominal reach width (e.g., W_{ra}). Line segments perpendicular to each centerline node are generated that intersect both banks (Figure 7d). The points of intersection of the perpendicular segments and the banks are found, and the channel width (W_{bl}) is computed as the distance between them. In cases where a perpendicular segment intersects more than two banks, only the two nearest intersections are kept. This method is beneficial for computing the river width at each centerline pixel but will not return the wetted width for multithread channels [cf. *Pavelsky and Smith*, 2008].

4.3. Migrated Areas, Cutoffs, and Erosion and Accretion

The RivMAP toolbox includes two methods for quantifying channel migration by measuring the areas traversed by the planform. Centerline and bankline migration areas are computed with the *migration_cl* tool, and erosional and depositional areas are obtained by planform mask differencing by the function *migration_ mask*. Both functions contain routines for separating cutoffs from migrated areas. The functions to quantify planform migration and identify cutoffs rely on image processing techniques rather than vector based [e.g., *Lauer*, 2006].

The *migration_cl* tool requires inputs of centerline or bankline coordinates obtained at different times, their exit sides, a nominal channel width (e.g., W_{ra}), and the size of the image from which coordinates were derived. Both centerline or bankline coordinates may be used, and they may be smoothed or not. A binary mask is created for both centerlines (Figure 8a). The areas to one side of each image are filled (Figures 8b and 8c) resulting in two images $I_{\mathrm{half},t1}$ and $I_{\mathrm{half},t2}$. An image of migrated area is computed by the union of the forward and backward difference of the images at times t_1 and t_2:

$$I_{M,cl} = \left(I_{\mathrm{half},t2} - I_{\mathrm{half},t1}\right) \cup \left(I_{\mathrm{half},t1} - I_{\mathrm{half},t2}\right). \tag{7}$$

A check ensures that the centerline at t_1 contributes no area to $I_{M,cl}$ and that the centerline at t_2 does, except for pixels where the centerline has not migrated (Figure 8e).

If the centerline undergoes cutoffs between t_1 and t_2, the cutoff areas will appear as migrated area in $I_{M,cl}$ and require separation. After finding the image of migrated areas, the RivMAP function *migration_cl* identifies cutoffs by thresholding the change in streamwise distance between centerline segments (Figure 9). First, all intersections between the centerline at t_1 and t_2 are found and ordered upstream-to-downstream. Each consecutive pair of intersections defines a segment; the centerline length of each segment is found for both t_1 and t_2 centerlines as follows:

$$\mathrm{seglen}_{j,t_1} = \sum_{i(j)}^{i(j+1)} ds_i \tag{8}$$

where $i(j)$ refers to the ith centerline node corresponding to the jth segment.

Cutoffs are defined by segments that were shortened by more than twice the reach-average channel width: $\mathrm{seglen}_{j,t_1} - \mathrm{seglen}_{j,t_2} > 2W_{ra}$. A binary mask is constructed from the t_1 and t_2 centerlines bounded by segments fulfilling this inequality. Migrated area maps of the Ucayali showed that cutoffs often featured "tails" of thin migrated area where adjacent bend migration areas connect to the cutoff area (see Figures 9c and 9d). These tails are disconnected by eroding the cutoff mask and keeping only the largest connected area. The eroded mask is then overdilated to ensure all actual cutoff area is retained, and the mask is applied to $I_{M,cl}$ to separate cutoff areas from migrated areas. The *migration_cl* function returns an image of migrated areas with cutoffs removed, an image of cutoff areas, the areas of each cutoff, and the cutoff indices along the t_1 centerline.

The *migration_mask* function in the RivMAP toolbox provides a way to quantify planform change through channel mask differencing. Mask differencing requires no centerline; thus, both multithread or single-thread masks may be used. Figures 8f–8i demonstrates the mask differencing procedure, including cutoff

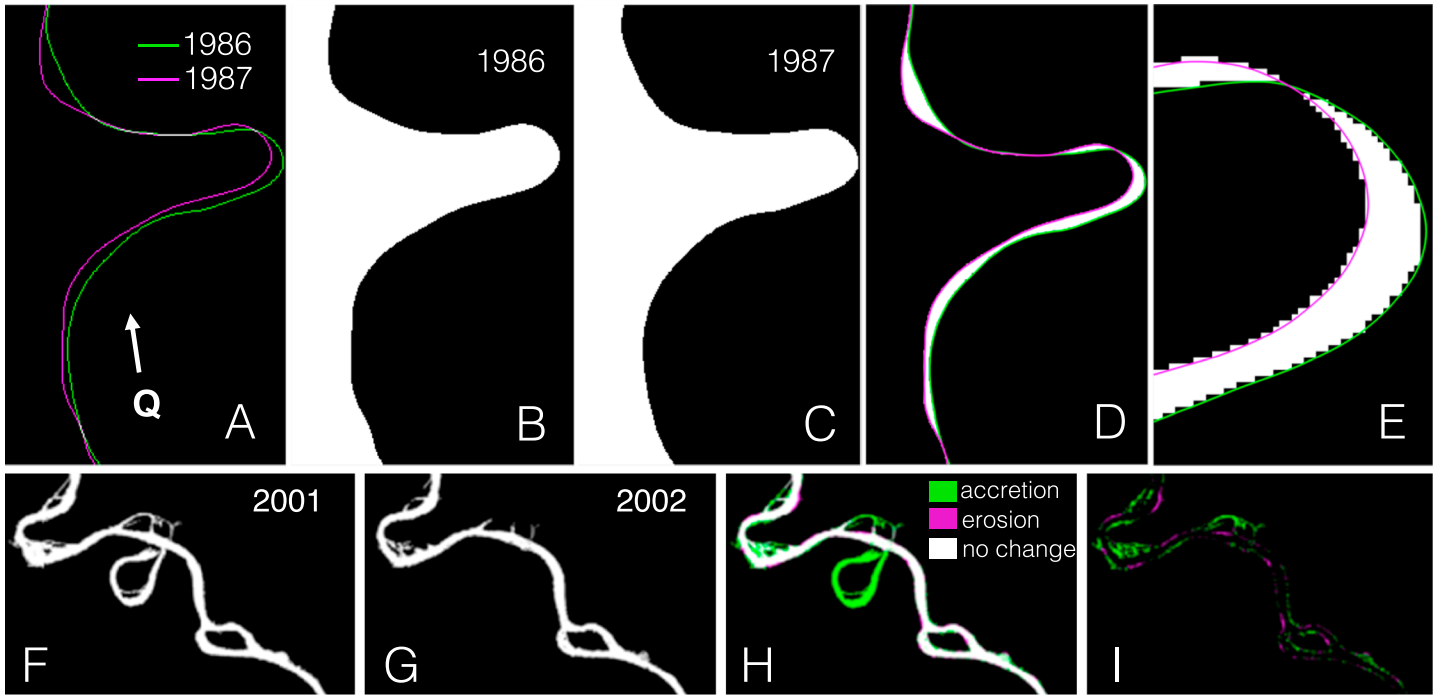

Figure 8. (a–e) The procedure for computing migrated areas from centerline or bankline is illustrated for a reach from R5. In Figure 8a, the centerlines at both times are shown. White pixels correspond to their overlap. The filled image halves are shown for 1986 (Figure 8b) and 1987 (Figure 8c), and the migrated area found by the union of their differences is shown by the white pixels in Figure 8d. A closer look at the migrated area (Figure 8e) confirms that the 1986 centerline does not contribute to migrated area, while the centerline at 1987 does. The migrated area reflects the modes of bend migration; the bend has translated downstream, rotated slightly, and shortened. In (f–i) Areas of erosion and accretion are obtained from differencing the hydraulically connected channel masks for a reach in R4. The masks for 2001 and 2002 are shown in Figures 8a and 8b, respectively. Erosion, accretion, and no change areas after mask differencing are shown in Figure 8c. Erosion and accretion areas after removing the detected cutoff are shown in Figure 8d.

detection. If the image of cutoff areas computed by *migration_cl* is provided, cutoffs are identified as accretional areas that overlap the cutoff areas image. Otherwise cutoffs are identified with a simple area threshold on the connected areas within the accretion image. For the Ucayali, a threshold of $3W_{ra}^2$ successfully discriminated between cutoffs and large patches of connected accretion areas (see Figures 8f–8i). If the elapsed time between two channel masks is large, it is possible that the channel may have migrated a distance larger than the local channel width, and RivMAP's basic mask differencing will underpredict areas of erosion or accretion [see *Rowland et al*., 2016]. Areas of erosion and accretion may also be more sensitive to uncertainties associated with classification of imagery; see the supporting information of *Rowland et al*. [2016] for a discussion. We note that RivMAP's mask-differencing technique is best suited for single-thread channels. For multithreaded channels, the SCREAM package [*Rowland et al*., 2016] provides comprehensive mask-differencing analysis that handles complexities imposed by islands and multidirectional flow paths.

4.4. Quantifying Changes in Space and Time

The main challenge in quantifying spatial changes lies in constructing a mesh of buffer polygons that include all channel positions through time, are roughly evenly spaced, and orient approximately normal to the channel belt axis. RivMAP's *spatial_changes* function requires all the images of migrated areas and channel positions as well as each of the individual centerline images found using *centerline_from_mask*. A desired spacing (D) over which to compute quantities is also required; this spacing is not related to the user-selected spacing to find channel widths. First, the channel belt boundaries are found by dilating the image of all channel positions and calling the *banklines_from_mask* function to return its edgelines. Each edgeline is "oversmoothed" with a first-order Savitzky-Golay filter [*Savitzky and Golay*, 1964] of window size $50W_{ra}$ to remove bend-scale edgeline variations while preserving the lower frequency channel belt meandering. A mask of the channel belt is then constructed from the oversmoothed banklines.

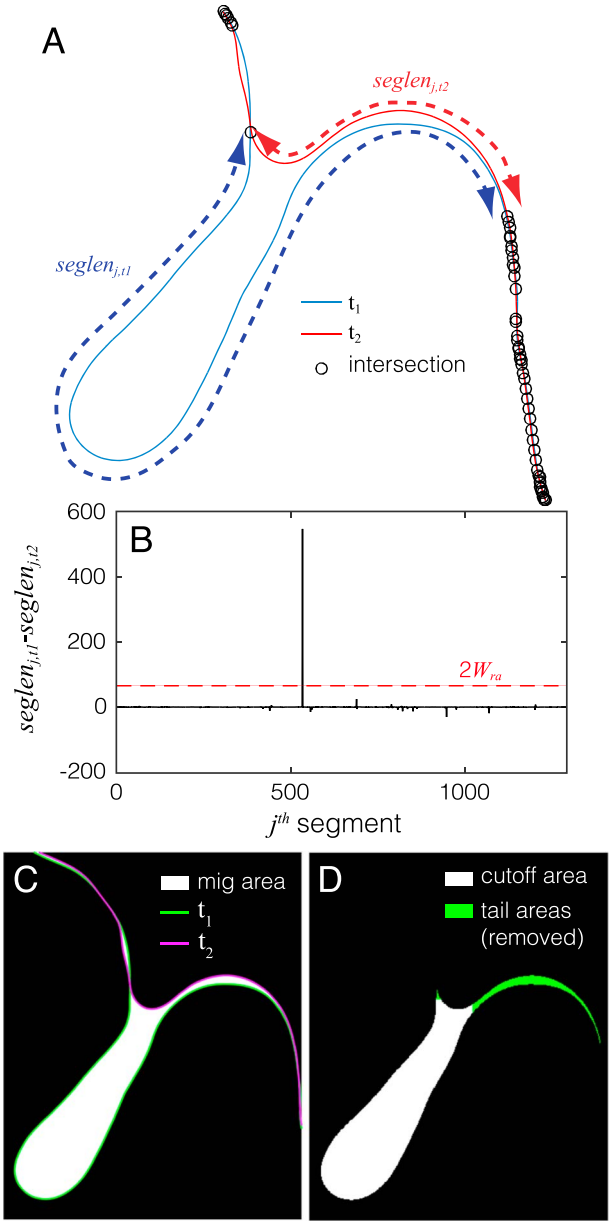

Figure 9. Procedures for identifying and trimming cutoffs are illustrated. (a) The centerlines of a cutoff bend from R5, 1987 and 1988, are shown with their intersections marked by circles. The segment lengths for the cutoff portion are defined. (b) The difference $seglen_{t1}$-$seglen_{t2}$ for each jth segment is plotted for the entire R5 reach, with the threshold for identifying cutoffs denoted by a dashed line. The peak in this plot at $j = 533$ corresponds to the cutoff bend in Figure 9a. The problem of tails is illustrated in Figure 9c, where the cutoff area is joined to migrated area. The cutoff area after tail removal is shown in Figure 9d.

The smoothing procedure typically decreases the width of the channel belt so that its boundaries no longer include all the channel positions. The procedure is thus repeated with dilations incrementally increased by $0.5W_{ra}$ until the mask overlaps all pixels of the all channel positions image (Figure 10a).

After the edgelines of the channel belt are found, they are coarsely resampled at intervals of $20W_{ra}$. The nodes of the coarsely sampled edgelines are used to construct an intermediate piecewise cubic spline, and the edgelines are resampled from the spline at a finer resolution ($0.1W_{ra}$), resulting in two densely sampled edgelines that have been smoothed via a third-order interpolant (Figure 10b). Resampling via piecewise cubic splines is necessary to provide a smooth curvature signal. An approximate centerline is computed as the average coordinate positions of the edgelines, and its inflection points are found by zero crossings of its curvature signal. Centerline inflection points are filtered such that each inflection is at least $3D$ away from the ends of the centerline and at least $3D$ away from the nearest adjacent inflection. For each inflection point, a line perpendicular to the centerline is intersected with each edgeline, thus matching each centerline inflection node with a corresponding left (pl_i) and right (pr_i) edgeline node. The number of buffer polygons ($n_{b,i}$) to create between each inflection point is computed as $(S(pc_{i+1})\text{-}S(pc_i))/ds$ where $S(pc_i)$ is the streamwise distance from the upstream end of the reach to centerline inflection point pc_i. Finally, each edgeline is again resampled from the piecewise cubic spline at intervals defined by $(S(pl_{i+1})\text{-}S(pl_i))/n_{b,i}$ and $(S(pr_{i+1})\text{-}S(pr_i))/n_{b,i}$ (see Figure 10c). The procedure results in buffer polygons that are roughly perpendicular to the larger channel belt, while locally the buffers themselves are wider along outer edgelines and narrower along inner edgelines (Figure 10e).

Buffer polygons are constructed by connecting each node of the left edgeline with its right edgeline counterpart and connecting each node to its nearest upstream and downstream neighboring nodes (Figure 10d). A mask is created from each buffer polygon and applied to each image of areas, returning a $Y \times n_b$ matrix where Y is the number of realizations (e.g., 30 years for this study). This matrix quantifies areal changes in space and

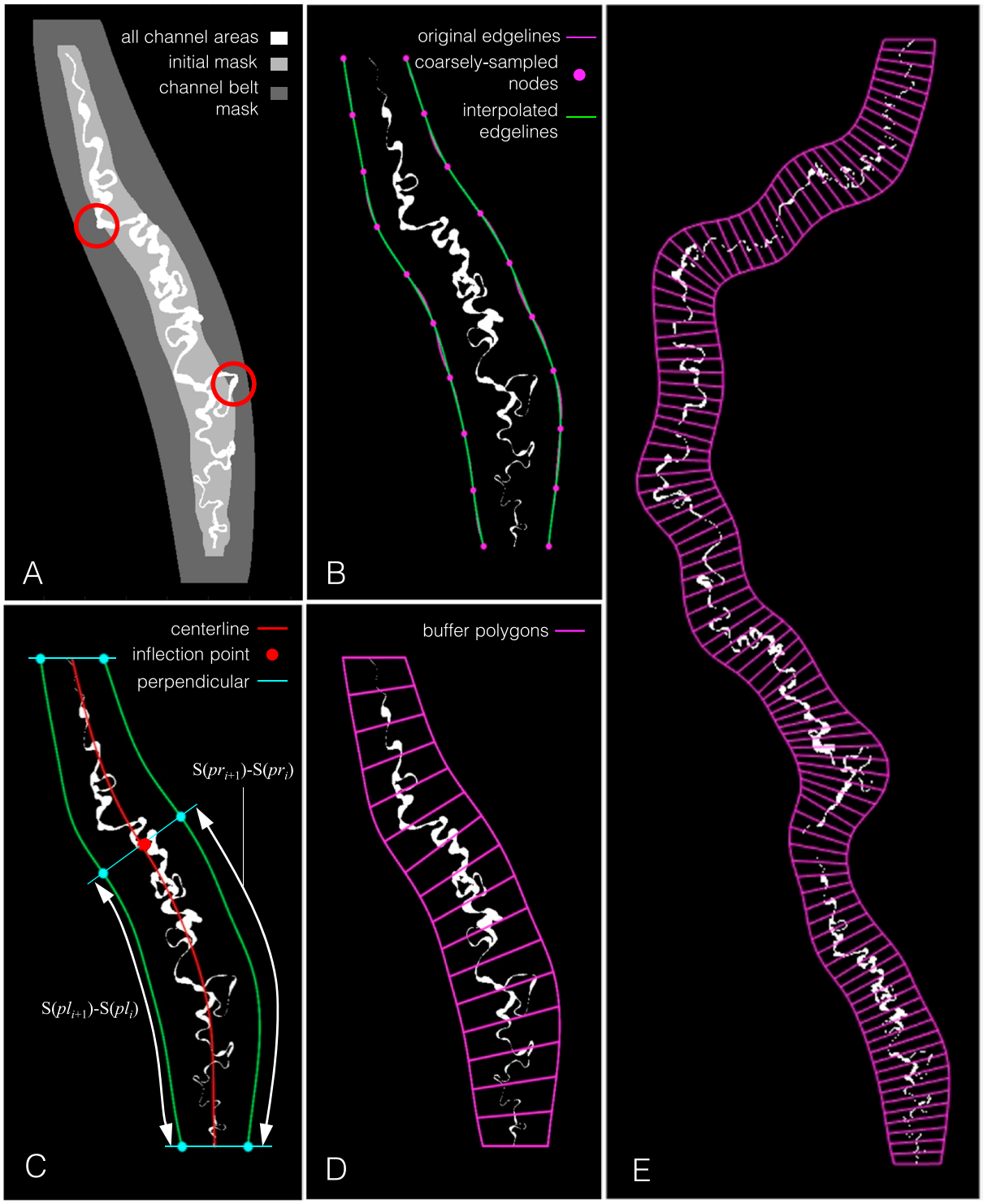

Figure 10. The procedure for defining a channel belt and creating buffer polygons to quantify changes spatially is illustrated. (a) All channel positions from R6 are shown from 1985 to 2015 in white. The initial channel belt mask delineated by oversmoothing the edgelines of the dilated channel mask image is in light gray. The two circles show regions where the initial mask does not capture all the channel positions. Dark gray shows the final channel belt mask that captures all migrated areas. (b) The original and coarsely sampled edgelines. (c) The channel belt centerline and its inflection point along with the definitions of the lengths used to resample each edgeline. (d) The final buffer polygons for R6 with a spacing of $3W_{ra}$ and for the (e) entire reach. Spacing in Figure 10e is $6W_{ra}$ for visualization purposes but can be reliably reduced nearly as far as the resolution of the input image.

time and can be plotted as a space-time map of planform changes (see Figure 14a). The average centerline length (l_{avg}) within each buffer polygon is also computed for normalizing dynamic metrics. The example shown in Figure 10 demonstrates centerline migrated areas, but areas of erosion, accretion, channel position, and sediment may be found with the tool.

4.5. Morphodynamic Metrics

While RivMAP provides tools for mapping and quantifying planform changes, it does not compute morphodynamic metrics. Users may define relevant metrics and readily compute them from RivMAP outputs. For example, images of bankline or centerline migrated areas obtained from the *migration_cl* or *migration_mask* tools may be used to compute migration rates over desired space and time domains. We define an average rate of migration for a reach by

$$M_{cl} = \frac{A_{cl}}{A_c(t_2 - t_1)} \times 100\% \tag{9}$$

where A_{cl} is the total migrated area traversed by the centerline, A_c is the area of the channel and M has units %/time. Normalization by the channel area removes dependence on both width and length, but migration rates may also be normalized by only centerline length [e.g., *Larsen et al.*, 2006].

Changes in channel length are quantified through sinuosity (η), defined by

$$\eta = \frac{l_{cl}}{l_v} \tag{10}$$

where l_{cl} is the river's centerline length and l_v is the valley length estimated by the length of the channel-belt centerline (defined in the previous section and Figure 10e) which does not change through time herein. Annual centerline growth is captured by the elongation rate (e_r) given by

$$e_r = \frac{l_{cl,t_2} - l_{cl,t_1} + l_{cut}}{t_2 - t_1} \tag{11}$$

where l_{cut} is the total length of cutoffs occurring between t_1 and t_2 (cf. "channel extension" metric of *Lauer and Parker* [2008]). RivMAP's tools permit the calculation of metrics for the full reach or within subreaches defined by buffer polygons (Figure 10e).

5. Results: The Morphodynamic Evolution of the Ucayali River

RivMAP was applied to the single-thread channel masks of the Ucayali River to quantify its annual morphodynamic evolution. The following subsections present quantified planform changes in length, width, erosional and accretional areas, and migration rates through the interpretation of space-time maps. Each space-time map was created by applying the buffer polygons shown in Figure 10e to the relevant reach-wide map of areas each year. The distance along the channel belt centerline was used to parameterize the downstream distance for the maps. Additionally, elevation, precipitation, and stage data were obtained to identify possible climatic and geologic controls on observed planform changes. This section concludes with an uncertainty analysis performed by applying the classifying, cleaning, compositing, and quantifying planform change techniques to three pseudostationary bends where planform changes were assumed to be negligible.

5.1. Centerline Changes Including Cutoffs

Annually resolved centerlines for over 1500 km of the Ucayali River from 1985 to 2015 created using RivMAP illustrate the complex and active morphodynamics of the river (Figure 11). Bends exhibited the gamut of migration modes including translation, expansion, extension, and/or rotation [*Daniel*, 1971]. Two mild-curvature bends (Figure 11, R5, right zoom) displayed nearly pure downstream translation with little deformation. Consistent with linear perturbation theory of meander development under subresonant conditions [*Ikeda et al.*, 1981; *Seminara et al.*, 2001], the length of most bends increased in time as meanders developed

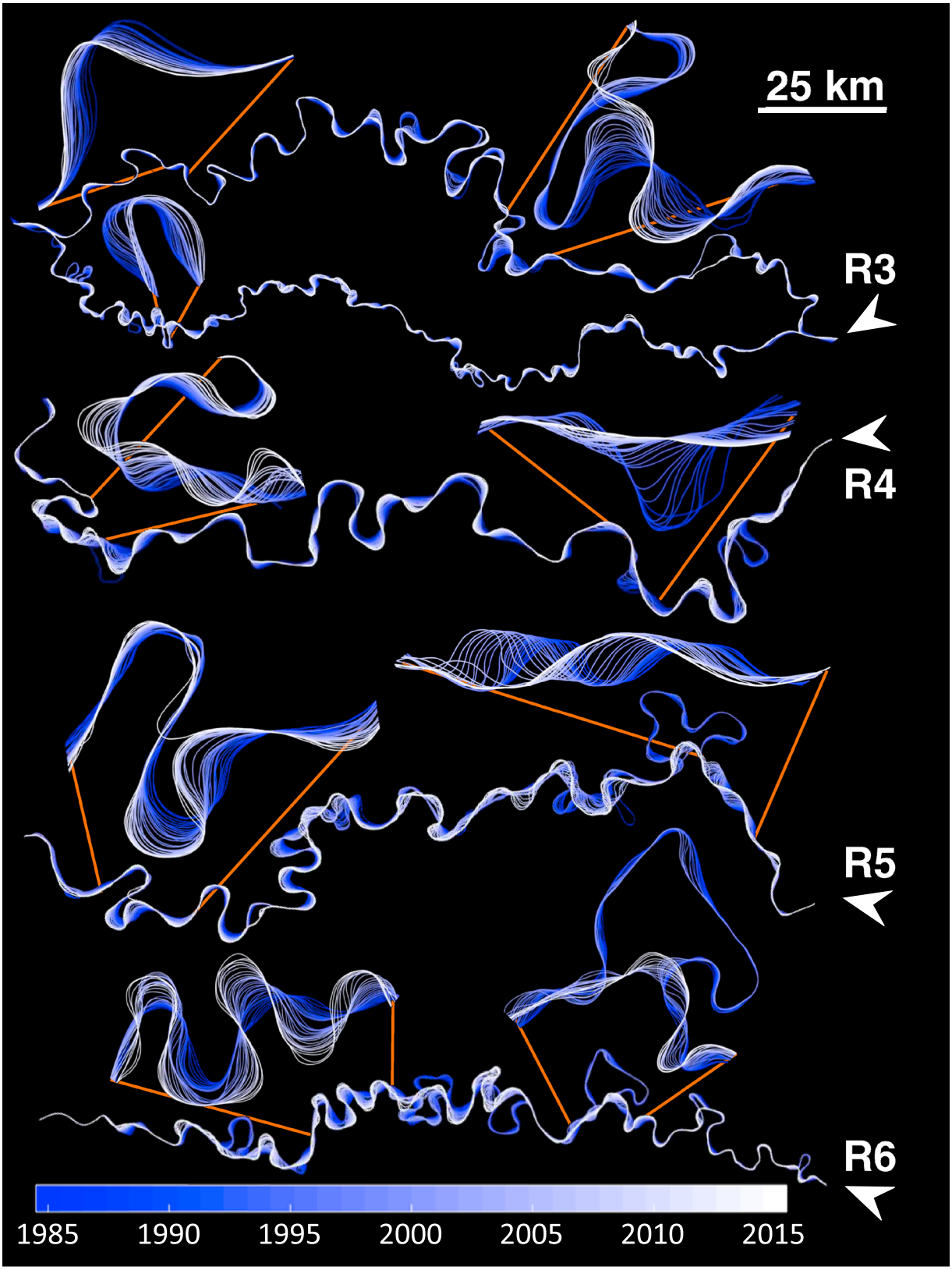

Figure 11. Centerlines obtained from Landsat-derived single-thread channel masks using RivMAP are shown for the study regions of the Ucayali. North arrows also indicate the direction of flow which travels from R6 to R3. Zoom views highlight some of the complex migration patterns and cutoffs along the Ucayali River. The total centerline length each year is approximately 1500 km including both branches in R3.

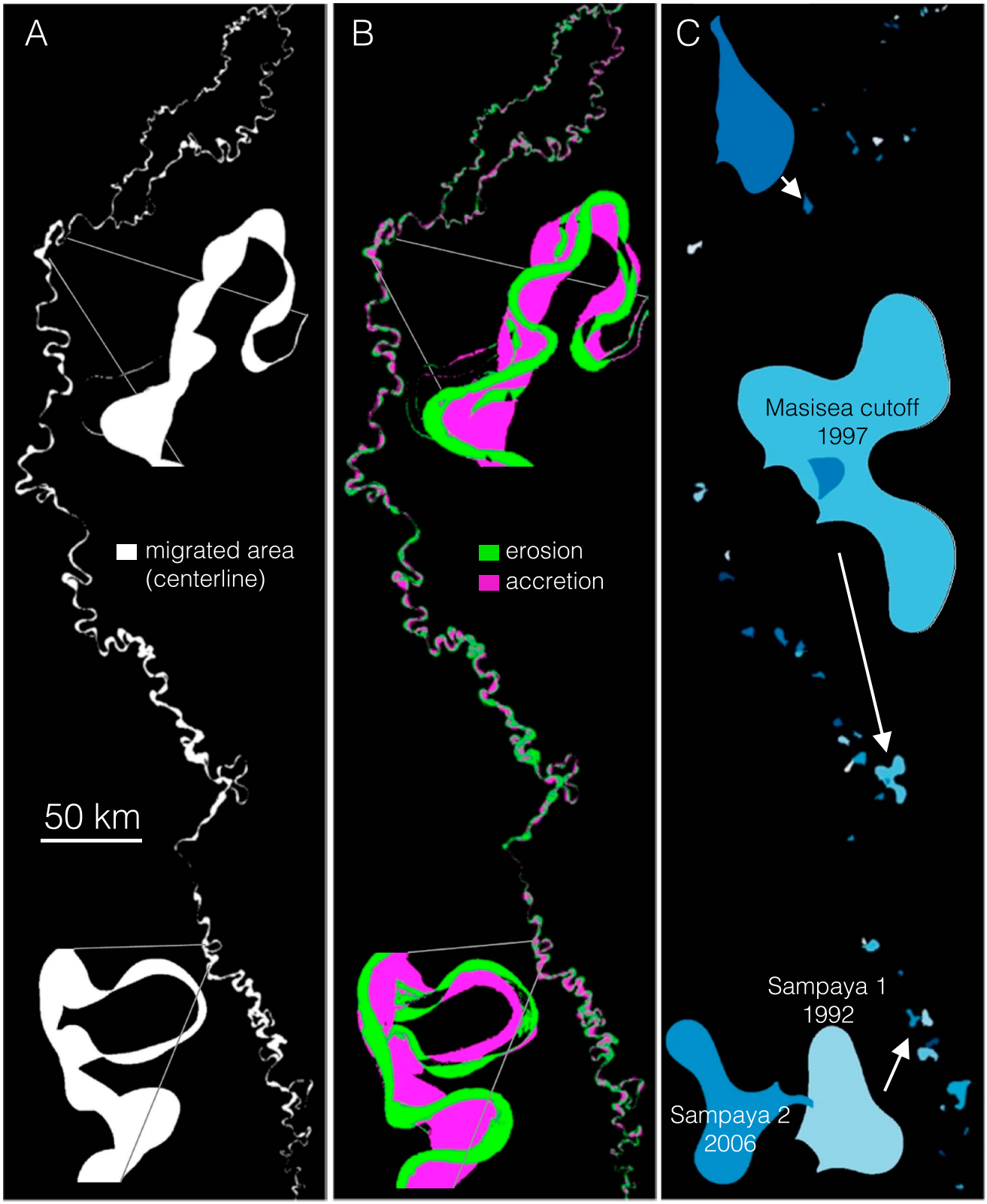

Figure 12. Migrated area and cutoff maps for the full study reach from 1985 to 2015 were computed using RivMAP. (a) Centerline migrated areas with two zoom views. (b) Erosion and accretion maps along with the same zoom views. A pixel may undergo multiple instances of erosion and/or accretion; only the latest occurrence is shown. (c) The 53 cutoffs that occurred from 1985 to 2015. Lighter cutoff areas occurred nearer 1985, while darker occurred nearer 2015. The longest cutoff within the study reach (Masisea) is shown in a zoom view, as well as the third and fourth longest (Sampaya 1 and 2).

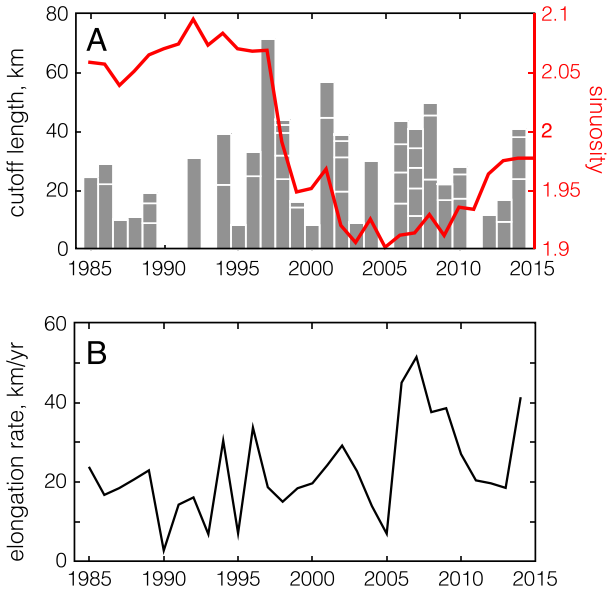

Figure 13. (a) Changes in the Ucayali River's centerline length across the 30 year period are illustrated by the sinuosity (red line) and cutoff lengths (bars). Breaks in the bars (white lines) for a given year indicate individual cutoffs which are arranged longest-to-shortest (bottom to top). The valley length was 683 km. (b) The rate of channel elongation for each year.

upstream-skew asymmetries. A notable exception is shown in Figure 11, (R4, right zoom) where a developed loop gradually devolved into a straight reach without cutoff.

From 1985 to 2015, 42 cutoffs occurred along the Ucayali River with a nearly equal number of chute and neck cutoffs (Figure 12c). Most cutoffs occurred in the upstream portions of the river (R6 and R5), although the northern bifurcation in R3 featured a number of smaller cutoffs. From 1985 to 1996, sinuosity fluctuated around 2.07, reflecting an apparent balance between channel elongation and the 14 cutoffs of the period. In 1997 the largest cutoff within the study area and period—a human-induced 73 km triple-lobed cutoff at Masisea—occurred near Pucallpa [*Abizaid*, 2005], overwhelming the river's elongation and leading to a sharp decline in sinuosity which achieved a minimum of 1.9 in 2005 following a series of smaller cutoffs. Despite the prevalence of cutoffs throughout the reach from 2006 to 2010, sinuosity rebounded to a 2015 value of 1.97. The occurrence of cutoffs did not necessarily decrease reach-wide annual sinuosity, as sinuosity depends on the balance between the cutoff rate and the elongation rate. For example, the cutoff rate from 1997 to 2002 (39 km/yr) was nearly equal to the 2006–2010 period (37 km/yr), yet the sinuosity declined 7% for the former and increased 1% for the latter. The discrepancy is due to greater elongation rates during the latter period (Figure 13b). The period of lowest sinuosity (2002–2010) was also the period with the highest elongation rates. The elongation rate of the Ucayali exhibited an overall increasing trend across the 30 year period, including a maximum rate of 51 km/yr, or about 4% of the centerline length per year.

5.2. Spatiotemporal Changes in Widths and Erosion/Accretion Areas

Average channel widths (W_{avg}) were computed annually using RivMAP's *width_from_mask* function to analyze the single-thread channel masks at intervals of approximately 3.5 channel widths (2.7 km) along the channel belt centerline. The space-time map of the Ucayali River's bankfull widths showed substantial multiscale variability (Figure 14a) around an average width of 825 m. Averaging width across time revealed a reach-scale trend of downstream widening (Figure 14b), with width at the bend-scale oscillating around this trend. In R3, where the river bifurcates into a northern and southern branch, the space-time width map indicated a shift in the river's primary flow path from the southern branch to the northern branch. The southern branch of the river in R3 (km 650–700) gradually narrowed while the northern branch widened (only the southern bifurcate is shown in the space-time map). This shift was also captured by the erosion/accretion map (Figure 12b) which showed a recently accreting southern branch complemented by an eroding northern branch.

Averaging width across space shows how the Ucayali River's width evolved over 30 years (Figure 14c). The bifurcated reaches of R3, beginning at a downstream distance of 540 km, were not included in the spatial averages due to the difficulty of aligning downstream distances for both reaches. Average reach-wide width decreased 72 m from 1985 to 1997, followed by an increase of 115 m from 1997 to 2015. Persistent channel widening at km 175–290 began in 1997, corresponding to the time and location of the largest cutoff in the domain (Masisea cutoff, 73 km long). Persistent channel widening also began in 2002 at km 60–100 following the second longest cutoff in the domain (Tumboya cutoff, 43 km long).

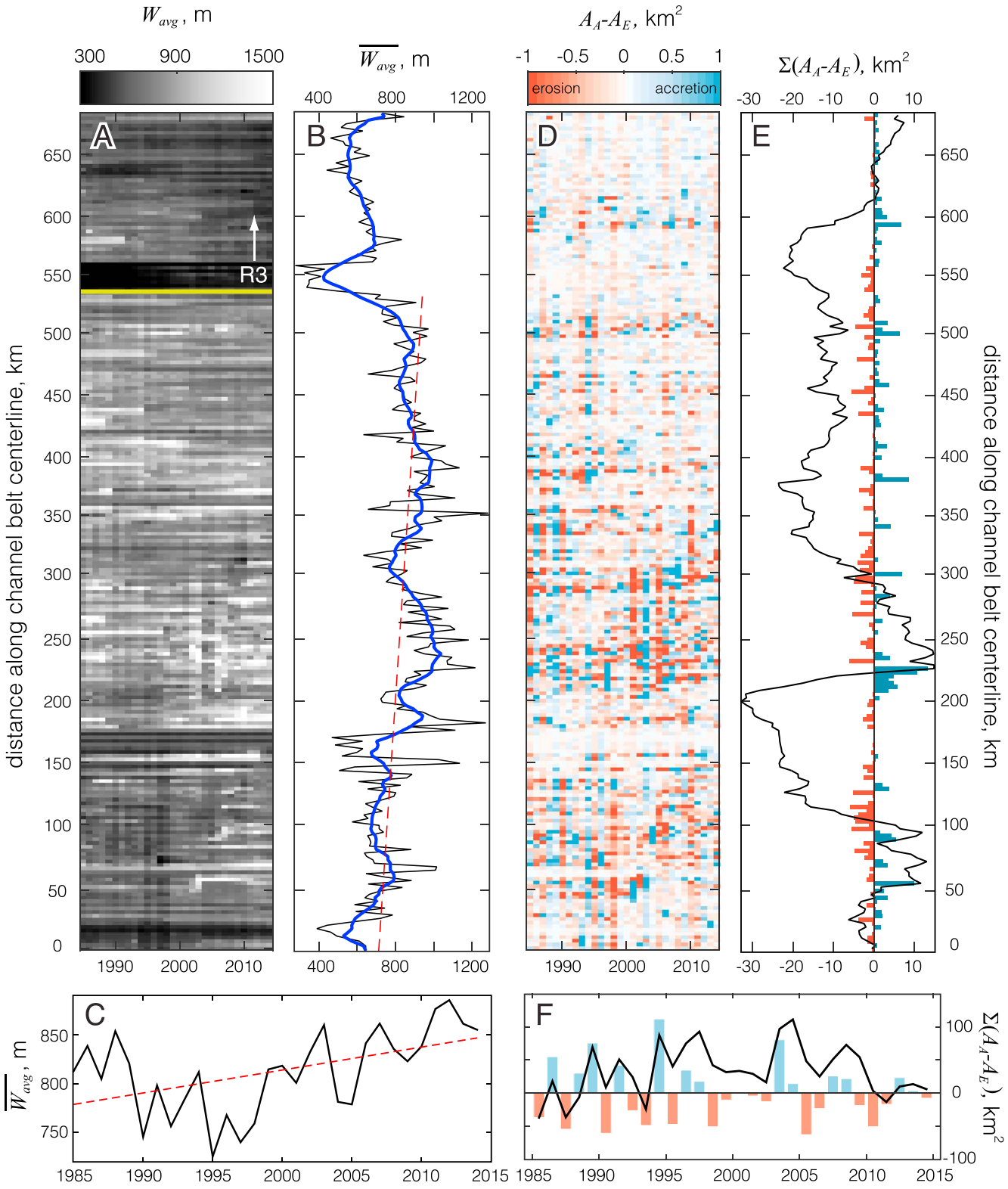

Figure 14. Space-time history of widths and accretion/erosion areas. (a) The space-time map of river width shows spatial and temporal width variability. The yellow line denotes the boundary between R4 and R3. (b) Averaging across all 30 years results in the spatial series of average widths. The blue line shows a smooth version, and the red dashed line shows the reach-wide trend. (c) The time series of average widths revealing an upward trend especially after 1990—a linear trendline (dashed red line) is overlaid for reference. (d) The space-time map of areas of accretion and erosion. (e) Summing areas across all times results in the bars. The black line shows the cumulative reworked area. (f) The time series of annual net erosion/accretion, with the cumulative area overlaid by the black line.

Channel width changes depend on the elongation rate and the balance between eroded and accreted areas. The space-time map of reworked floodplain areas depicts this local annual balance of erosion and deposition (Figure 14d). Approximately 82% of locations featured persistence times, defined as the duration an area remains erosive or accretive, of less than 2 years; 55% switched after only a single year. Persistence through space was more prevalent, where the average persistence length was roughly 17 km of river centerline length (28 channel widths).

Summing the eroded and accreted areas across 30 years revealed the spatial variability of local areas of floodplain growth and loss (Figure 14e). No downstream trend toward erosion or accretion was detected for the full reach, though significant reach-scale variability was observed. The downstream cumulative reworked areas revealed significant aggradation over a short distance surrounding the Masisea cutoff followed by a prolonged region of net erosion. A similar pattern was noted near the Tumboya cutoff, although to a lesser degree.

Overall, the spatial balance of reworked floodplain areas across the reach exhibited very little net erosion or accretion despite local sustained imbalances between accretion and erosion. The time series of reworked areas reflected a similar temporal balance over the 30 year period (Figure 14f). The short persistence times of accretion and erosion observed locally in the space-time map were expressed in the annual sums as well. Reach-wide floodplain reworking switched from net erosion to accretion, or vice versa, at most every 2 years. Cumulative reworked area through time showed that relative to 1985, the river was net erosional for only 4 years, primarily due to large accretions in 1994 and 2003. However, by 2010 the cumulative reworked area returned to zero after a 15 year period. Both spatially and temporally, the study domain and period were large enough to capture decadal and reach-wide cycles of net erosion and accretion.

5.3. Spatiotemporal Distribution of Migration Rates

Locally, reaches along the Ucayali have migrated as much as 750 m per meter of centerline in a single year, while other reaches have barely moved over 30 years. The space-time map of annual migration rates (equation (11)) showed a large migration hot spot sustained throughout the full 30 year period (km 70–120) and another spanning 1997–2015 (km 200–270, Figure 15a). Due to these hot spots, an overall trend of decreasing migration rates was observed in the downstream direction for the full reach. Neglecting the hot spots, a decreasing downstream trend of small magnitude persisted downstream of the hot spots (Figure 15b). Within the hot spots, local migrated areas exceeded up to 40% of the total channel area for some years. On average, the Ucayali River's centerline traversed 5.9% of the local channel area per year, or 1.6 m per centerline length. Curiously, between the two hot spots lied a reach of river that remained nearly stationary across 30 years (km 160–175). This dead zone consisted of two mild curvature bends that were 35% narrower than the average reach width and displayed almost no exposed in-channel sediment throughout the period. High-resolution imagery revealed no apparent human modifications to the banks or floodplain. A second shorter reach (km 360–363) exhibited similar characteristics of stationarity, narrowness (20% smaller than average width), mild curvature, and no bars. Averaging migration rates over space provided the temporal evolution of reach-wide migration rates (Figure 15c) and showed an increasing trend across the 30 year period, largely due to the hot spots near the Masisea (1997) and Tumboya (2002) cutoffs.

A Shuttle Radar Topography Mission (SRTM)-derived digital elevation model (DEM) of the Ucayali River (Figure 15d) showed that the two migration hot spots received sediment inputs directly from the nearby Shira Range. The southern (upstream) hot spot lied directly to the eastern face of the steep Shiras, while the northern hot spot was immediately downstream of the Pachitea River tributary which drains the western slopes of the Shiras. The Pachitea River alone accounts for 17% of the Ucayali's suspended sediment load immediately downstream its confluence [*Santini et al*., 2015]. The dead zone of migration (km 160–175) between the hot spots corresponded to the tapering off of the Shira Range. A slope profile generated from SRTM elevations (Figure 15b) showed a locally steep channel within the dead zone contrasting with the milder slopes of the hot spot reaches.

5.4. Climate Influence on Planform Changes

The Ucayali River is relatively data sparse, but available regional precipitation records and local stage recordings provided clues toward identifying climatic controls on planform changes reach wide. In the absence of direct discharge measurements, regional precipitation depths were obtained from *Lavado Casimiro et al*.

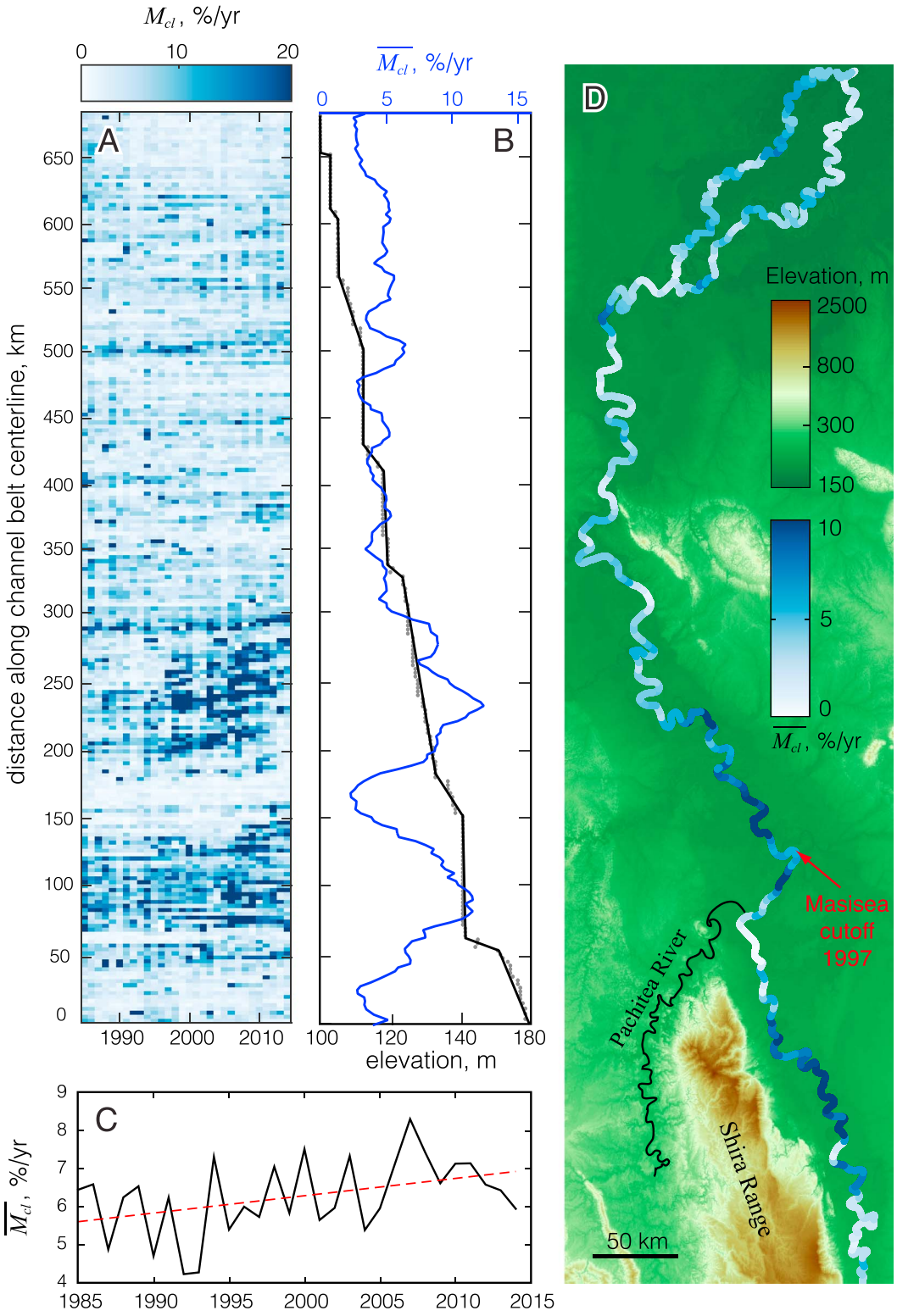

Figure 15. Space-time history of migration rates. (a) The space-time plot of centerline migrated areas normalized by channel areas (M_{cl}). (b) Migration rates averaged over 30 years ($\overline{M_{cl}}$) show the spatial variation in migration rates, blue line. The SRTM-derived elevation profile is also plotted in Figure 15b. (c) The time series of average migration rates is shown along with the linear trendline (dashed red line). (d) The 2015 centerline is plotted on top of a DEM and colored by average migration rate across the 1985–2015 period.

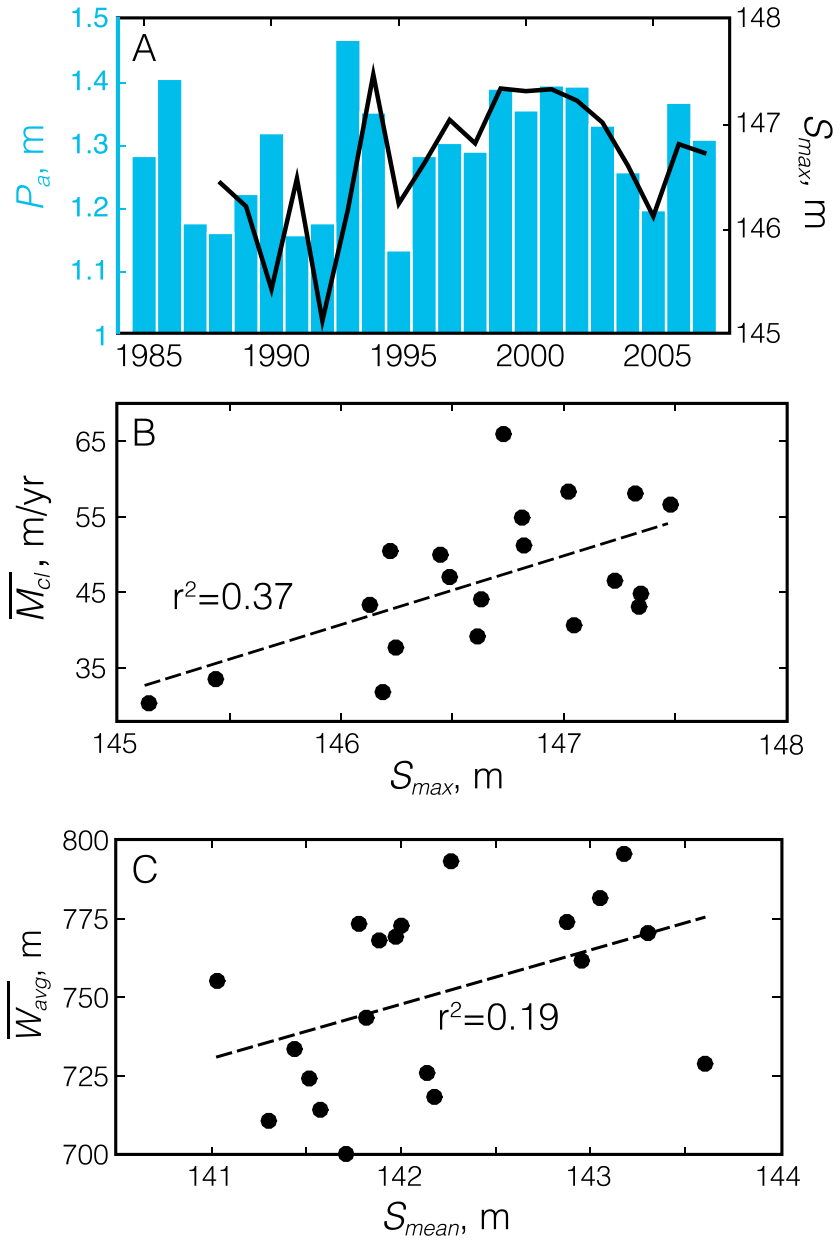

Figure 16. Climate-planform changes relationships. (a) Annual precipitation (P_a) values are shown as blue bars with the maximum annual stage (S_{max}) recorded at Pucallpa (km 238) overlain. Stages are reported in meters above sea level. (b) Annual centerline migration rates ($\overline{M_{cl}}$) are plotted against the maximum annual stage. (c) Annual reach-averaged channel widths ($\overline{W_{avg}}$) are plotted against mean annual stage (S_{mean}).

[2013]. Annual precipitation (P_a) aggregated from 77 stations was reported for the combined Ucayali and Huallaga basins, but the Ucayali basin accounted for 82% of the total measurement area. Stage measurements recorded at Pucallpa (km 238) offered a more direct estimate of discharge. Stage recordings are imperfect surrogates for discharge, as they incorporate morphologic changes of the river adjusting its depth to sediment and water fluxes, but the imprint of basin-wide precipitation was evident in both the mean and maximum annual stages which closely followed annual precipitation depths (Figure 16a). Maximum annual stages (S_{max}) were plotted against annual reach-wide migration rates ($\overline{M_{cl}}$) to assess the influence of climate on channel migration (Figure 16b). Migration rates were normalized by channel length rather than area to avoid dependence on channel width. Annual average migration rates showed slightly more dependence on maximum annual stage ($r^2 = 0.37$) than mean annual stage ($r^2 = 0.29$, not shown). In contrast, variations

Table 2. Uncertainty Estimates Obtained by Applying RivMAP to Three Abandoned, Nonactive Bends[a]

	Length (Pixels)		W_{avg} (Pixels)		M_{cl} (Pixels)		Erosion Rate (E) (Pixels)		Accretion Rate (A) (Pixels)	
	Mean (SD)	Range	Mean (SD)	Range	Mean (SD)	Maximum	Mean (SD)	Maximum	Mean (SD)	Maximum
Bend 1	451 (1.6)	7.2	21 (0.4)	1.4	0.34 (0.09)	0.50	0.71 (0.47)	2.0	0.83 (0.54)	2.5
Bend 2	222 (1.7)	6.6	19 (0.5)	2.1	0.32 (0.06)	0.44	0.46 (0.20)	1.0	0.73 (0.53)	2.3
Bend 3[b]	222 (1.1)	4.5	18 (0.7)	3.7	0.26 (0.20)	0.89	1.0 (2.1)	12	1.0 (1.1)	5.8
Bend 3[c]	221 (1.0)	3.8	19 (0.3)	1.1	0.20 (0.8)	0.34	0.63 (0.46)	1.4	0.77 (0.59)	2.3

[a]Statistics are computed for 30 years of annual composite-derived channel masks. Centerlines were not smoothed. W_{avg} was found by averaging W_{bl} across all centerline nodes. Centerline migration, erosion, and accretion areas were normalized by centerline length to calculate rates.
[b]Statistics include 2 years containing misgeoreferenced imagery.
[c]The misgeoreferenced years were removed.

in annual average channel width ($\overline{M_{avg}}$) exhibited no dependence on maximum annual stage ($r^2 = 0.01$) but were partly explained by the mean annual stage (S_{mean}, $r^2 = 0.19$, Figure 16c).

5.5. Quantifying Uncertainty of Planform Quantities

Uncertainty depends on the quality and resolution of the planform mask which integrates errors in geolocation, classification, and cleaning. Uncertainty bounds for planform variables measured by RivMAP were estimated by analyzing three abandoned bends annually from 1985 to 2015 following the procedures previously described. The bends were disconnected from the main river channel but were fed by small ($<0.1W_{bend}$) tributaries. The planforms of bends were assumed to be stationary, although fluctuations in their stages and therefore their planforms may have occurred due to climate fluctuations or flooding. Conservatively, any measured planform changes of the bends were interpreted as systemic error. The bends were selected to sample various potential sources of uncertainty; Bend 1 was adjacent to a city (Pucallpa) that required separation each year, Bend 2 was highly obstructed by clouds and stripes of scan line corrector-off bands for many years, and Bend 3 contained misgeorectified images in 1985 and 1987. The classification of sediment may also contribute significantly to errors in resolved planforms. However, the bends contained no exposed sediment so these errors are not represented. No stationary reaches with exposed sediment could be identified.

Table 2 shows that errors in planform variables were small relative to the 30 pixel width of the Ucayali River. However, Bend 3 demonstrated that measurements obtained from Landsat-based composites were highly sensitive to improperly georectified imagery. Errors in migration metrics were especially sensitive, as they are manifested in both the time when they appear as well as the succeeding time when the error was no longer present. In the absence of improperly georeferenced imagery, the maximum error for width was 2.1 pixels with a standard deviation of 0.5 pixel. Maximum errors for migration rates computed from migrated centerline areas, eroded areas, and accreted areas were 0.5, 2.0, and 2.5 pixels, respectively. Centerline migration errors were lower than mask-differenced erosion/accretion errors due to the relative insensitivity of the centerline to spurious clouds or misclassified pixels along the channel mask boundaries. The errors estimated here do not reflect the full extent of potential errors across the full study area, but they provide an estimate for the typical sources of uncertainty. Analysis with RivMAP requires no input parameters other than a nominal channel width used to generate buffer boxes and parameterize cutoff threshold area, so these errors reflect uncertainties associated with classifying and compositing Landsat imagery.

6. Discussion

Our analysis of the dynamic Ucayali River demonstrates the need for high spatiotemporal resolution snapshots of channel planform morphodynamics to adequately contextualize the observed migration rates and patterns within local to reach-scale planform dynamics. The remarkable multiscale spatiotemporal variability of planform evolution along the Ucayali River implies multiple controls on change. Two migration hot spots and a dead-zone fed (or starved) by sediment loads along the Ucayali demonstrate a nonuniform spatial control on migration rates imposed by local sediment inputs from the Shira Range [see also *Santini et al.*, 2015]. The identification of localized sediment-driven migration complements the work of *Constantine et al.* [2014] who identified sediment supply as a driver of channel migration on a reach-averaged basis for 18 rivers

within the Amazon basin. However, the spatial variability of migration rates along the Ucayali implies that reach-averaged migration rates depend significantly on the averaging domain.

Resolving planform morphodynamics with high spatiotemporal-resolution is critical toward identifying cutoff and climatic controls on planform changes. Without annually resolved migration rates, the abrupt increase of migration rates in 1997 within the downstream (northern) hot spot would not have been detected. The Masisea cutoff of 1997 was implicated in initiating this hot spot by releasing a sediment pulse during chute channel formation [*Zinger et al*., 2011], perturbing the local channel slope [*Biedenharn et al*., 2000] and/or increasing the downstream sediment flux through hydrologic synchronization effects [*Lane*, 1947]. However, sustained elevated discharge for nearly a decade beginning in 1996 may have affected the cutoff as well as the subsequent hot spot. Further analysis of 12 cutoffs distributed across the 30 year period and throughout the reach revealed significant accelerated migration rates downstream of 11 of the cutoffs and channel widening downstream for eight cutoffs [*Schwenk et al*., 2015a; *Schwenk and Foufoula-Georgiou*, 2016]. Cutoffs thus impart an additional control on nonlocal planform morphodynamics that, as in the case of the Masisea cutoff, may be amplified by local sediment inputs. The upstream (southern) hot spot was not initiated by cutoffs, but three major cutoffs augmented planform changes within the reach.

In addition to simultaneous sediment and cutoff controls on planform morphodynamics, climate influence is also apparent. Over the 30 year period, reach-wide migration rates, widths, and elongation rates showed increasing trends in conjunction with trends of greater precipitation and discharge. At the annual time scale, maximum annual floods exerted a greater degree of control on annual reach-wide migration rates than average flows. A similar relationship between maximum flows and channel activity was reported for the Rio Beni [*Gautier et al*., 2007]. We expected some dependence of channel width on the annual maximum flood which, when large can sweep away vegetation on established point bars and when small allows vegetation to reestablish [*Puhakka et al*., 1992]. However, annual variations in channel width exhibited no dependence on maximum annual floods, but some on annual average flows suggesting that annual flood persistence may be partially responsible for annual variations in width [see also *Martinez and Le*, 2007].

Annual snapshots of the Ucayali's planform fill in gaps that would otherwise exist from coarser time resolution, offering a clearer view of the river's dynamic adjustments. Following a major decline of sinuosity, the river responded by gradually widening over the following decade and lengthening at a quicker pace. The biennial cyclicity of reach-wide net erosion followed by accretion shows how the river maintains balance despite changes in sediment supply, cutoffs, and climate. In the bifurcated portion of the river, our analysis revealed the narrowing of the southern branch in conjunction with the widening of the northern one, capturing the gradual shift of the primary flow path between the two bifurcates.

The primary source of uncertainty in our analysis stems from misgeoreferenced Landsat imagery which can affect large reaches if unaccounted. In 2016, the USGS announced a reprocessing of all Landsat imagery geolocation errors (http://landsat.usgs.gov//about_LU_Vol_10_Issue_1.php), but the corrected Landsat products were not available at the time of this study. Our focus on the primary channel of the Ucayali may also overlook important morphodynamic contributions of secondary channels to width, erosion, and accretion. Secondary channels removed during conversion to single-thread masks may result in underpredicted widths, especially in rare cases where the primary and secondary channel widths are comparable. However, our estimate of the Ucayali's average bankfull width (825 m) is greater than previously reported remotely sensed Ucayali widths ranging from 600 to 700 m [*Kalliola et al*., 1992; *Constantine et al*., 2014]. Our uncertainty analysis shows a maximum centerline migration rate error of 0.5 pixels/yr (15 m/yr), which is 30% of the reach-wide average rate across our time period. Without improvements in Landsat data georeferencing or classification, care should be taken in applying our techniques to smaller and less active rivers where migration rates may be of similar magnitude to maximum errors.

7. Conclusions and Future Work

This study offered a framework for mapping and quantifying planform changes of large, active meandering rivers at high spatiotemporal resolutions. Through mapping of annual planforms at Landsat-pixel scale of 30 m, our results provide a basis for determining controlling factors on local planform changes and contextualizing them within the broader reach. Insufficient temporal resolution can miss key processes such as the role of cutoffs as drivers of nonlocal morphodynamic changes. Our framework brings us closer toward

understanding how rivers in natural settings may author their own geometries by adjusting in response to both autogenic (e.g., cutoffs) and allogenic (e.g., climate) forcings.

We also introduced the RivMAP toolbox, which provides intuitive, easily customized, and parallelizable MATLAB codes for analyzing meandering river masks derived from satellite imagery, aerial photography, historic maps, or DEMs. By taking advantage of MATLAB's efficient image processing functions, RivMAP tools quantify widths, centerlines, banklines, centerline migrations, and erosion and deposition rates over large spatial domains using a personal computer. Once clean binary masks were obtained, computing these quantities for 1500 km of the Ucayali River required less than 2 h on a quadcore laptop. The tools themselves are easily parallelizable across time and space with MATLAB's *parfor* command for application to larger data sets. The Ucayali River was particularly challenging due to its complex migration patterns, numerous secondary channels, and pervasive cutoffs, and RivMAP was designed around these complications. RivMAP's centerline-centric approach renders it most useful to studies of single-thread channels, but RivMAP also contains basic functionality to quantify planform changes for multithreaded channels.

Based on estimates of uncertainty associated with classifying and compositing Landsat data, our techniques can provide meaningful annual morphodynamic insights in large and/or highly active rivers from Landsat imagery. With current Landsat data, over a dozen large, tropical meandering rivers, e.g., the Mamoré, Beni, Juruá, Fly, and Sepik Rivers, are ideal candidates for quantifying morphodynamic changes and identifying process controls on planform adjustments from Landsat imagery. Although not analyzed in this work, our composite images resolve in-channel sediment dynamics through planform views of bars exposed at low stage, permitting research of the effects of bar morphology on planform dynamics. Further study is underway to more fully understand the effect of cutoffs as perturbations to migration rates, characterize floodplain residence times and dynamics, and link meander migration to planform morphology.

Appendix A: Compositing Procedure

An image bank was constructed for each year by selecting only the images from within the 1 June through 31 October window. For each year, each image in the bank was plotted, and N images with properly classified and clear views of the river were selected for inclusion in the composite. N ranged from 2 to 11; larger N was required for composites where cloud cover obscured the view of the river in many images. In order to minimize the accumulation of errors inherent in Landsat imagery and the classification process [*Adams et al.*, 1993; *Lu et al.*, 2004], no more than four clear views of the river were used to create a composite. With the exception of a section of R3-1990, the 5 month search window was sufficient across all scenes and dates to create a reliable composite image.

The compositing algorithm gave preference to sediment pixels to maximally resolve in-channel and point bars. The N images were combined into a single $P \times N$ stack where P is the number of pixels each image contains and a $P \times 1$ composite image was initialized with zeros. Each pth pixel in the composite image was assigned according to a hierarchical scheme that gave preference to sediment, followed by water, land, and finally cloud classes. For example, if any of the N pixels in the pixel stack were classified as sediment, the composite image's pixel would be set as sediment. If not, the stack was checked for water, followed by land, and finally clouds. An example of the compositing process is shown in Figures 5a–5d.

For each composite image, a corresponding datemap was also created by storing the date of the image that each pixel was drawn from. If, for a pixel, more than one image in the stack of N were the same class as the final composite class, the image whose date was nearest to the center of the search window was selected as the datemap value. Datemaps show the relative contributions of each image to the final composite; Figure A1 shows the date compositions of only the channel masks. For the R3 and R5 boxes, no image from a single date could cover the entire river because it crosses Landsat paths. Thus, these boxes required approximately twice the number of images to create a single composite. In R4, over 70% of each composite was contributed by a single image except for 1990, 2002, and 2012. In R6, exceptional cloud cover necessitated more individual images to create composites.

The compositing procedure was developed iteratively. Initially, compositing was performed using all available images within the 6 month window to create the image stack. More sophisticated algorithms were initially developed to determine the composite pixel class from a pixel stack; for instance, the composite pixel

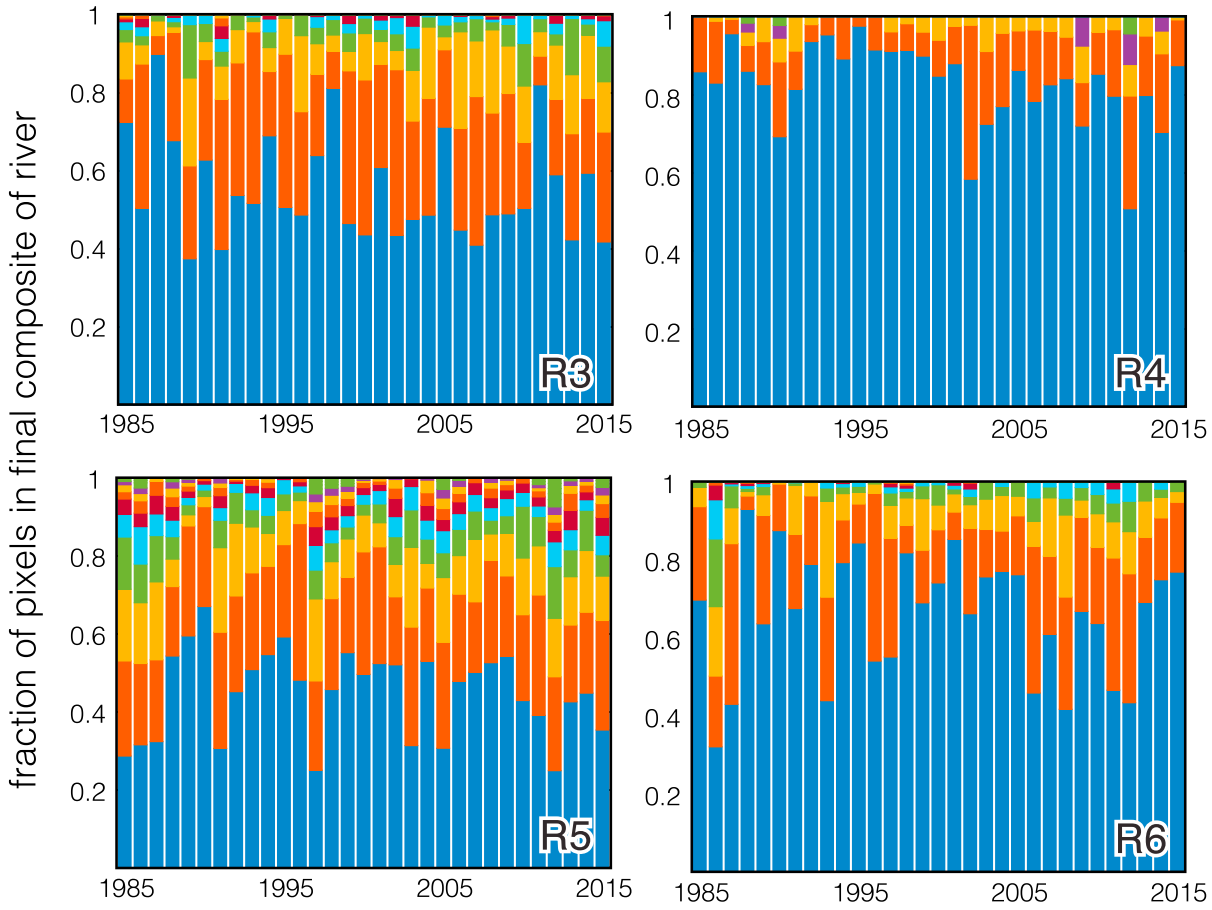

Figure A1. The contributions of pixels from individual classified images to the final composite river mask are shown for each year within each R box. The *y* axis represents the number of pixels contributed divided by the total number of pixels in the binary channel mask. Each color represents a different individual image; the number of colors for a given year corresponds to the number of images that contributed to resolving the channel. Contributing image fractions are sorted from largest to smallest (bottom to top). The color scheme repeats after six colors.

would be sediment class only if >30% of the pixels in the stack were sediment. This methodology was robust against improperly classified pixels, but it failed to resolve the bankfull channel for cases where few full, clear scenes were available. The simpler method we employed resulted in noisier composites (e.g., where clouds are misclassified as sediment, they show up as sediment in the composite) but required fewer images to create a representative composite. As a result, the composites required additional cleaning described in section 3.

Appendix B: Manually Cleaning Channel Masks

In addition to problems described in section 3, cleaning is also important to ensure consistency across imagery. For example, consider quantifying erosion and deposition by differencing composite-derived channel masks at different times. If a composite contains a chute channel at t_1 but not at t_2 due to poor Landsat imagery, but the chute is again detected at t_3, its absence at t_1 will appear as deposition, and its reemergence at t_2 will be considered erosion, while no erosion or deposition actually occurred.

Each composite image was manually cleaned by removing all connected components that were not hydraulically connected to the river (i.e., tributaries, cities, misclassified clouds, and cutoff remnants). First, a binary mask of the composite was created from the water and sediment pixels. This mask was plotted alongside the original composite image for reference, and the areas not connected to the main river body were removed. In order to achieve consistency across the cleaned images, the cleaned binary image from the previous time step was superimposed onto the image being cleaned. The most common cleaning procedures included the removal of tributaries, cities, and misclassified clouds and the filling of missing data due to insufficient

Landsat imagery, cloud cover, or SLC-off bands. Hand interpolation because of missing data was required for only a few composites, and interpolations were over distances less than a channel width. The result after cleaning was stored as a binary image containing all the hydraulically connected area of the main channel.

Cleaning was performed using RivMAP's *hand_clean* function, which allows the user to create a mask from a hand-drawn region of interest (ROI). After drawing an ROI, its class (e.g., water, sediment, and land) was defined by a numeric input, and further ROIs were drawn and reclassed until cleaning was complete. The hand cleaning process was the most time-consuming step of this study and could be improved or eliminated with a refined classifier, more Landsat imagery, and/or a pathfinding algorithm that follows the main channel banklines.

Following cleaning, a single-thread channel mask was created by selecting the primary river path at each bifurcation. In order to determine the active channel in a multithreaded portion of the river, channel width and temporal consistency were prioritized. As avulsions or chutes gradually emerged from a bend, imagery from the next several years was referenced to ensure a consistent channel devoid of artificial jumps in the centerline. For example, in many meander bends a "tip cutoff" would occur where a smaller chute channel would bypass only the apex of the meander bend as opposed to cutting across the bend's neck. Though narrower initially than the meander bend tip, this chute channel would grow through time and eventually coalesce with the bend tip. If the chute channel became wider than the bend during its evolution, it was considered the main path of the river throughout all times. Similarly to the cleaning procedure, creating a single-thread mask was performed with the mask from the previous time superimposed to ensure consistency of path selection. The resulting image after path selection was stored as a binary image of the dominant, single-thread river path.

Acknowledgments
This research benefitted from collaborations made possible through the NSF grant EAR-1242458 under Science Across Virtual Institutes (SAVI): LIFE (Linked Institutions for Future Earth). Funding was also provided by NSF grant EAR-1209402 under the Water Sustainability and Climate Program (WSC): REACH (REsilience under Accelerated CHange). J.S. acknowledges support provided by an NSF Graduate Research Fellowship. Eric McCaleb, Mace Blank, and Anuj Karpatne of the University of Minnesota's Computer Science Department provided assistance obtaining and classifying Landsat imagery of the Ucayali River. We also appreciate thoughtful reviews from Burch Fischer, Tamlin Pavelsky, and Joel Rowland. We thank Christian Abizaid at the University of Toronto, St. George, for providing stage data at Pucallpa, Peru. Landsat imagery was acquired from the Google Earth Engine API. RivMAP files, including a demo, walkthrough, and sample data, are available at the Mathworks File Exchange: https://www.mathworks.com/matlabcentral/fileexchange/58264-rivmap-river-morphodynamics-from-analysis-of-planforms.

References

Abizaid, C. (2005), An anthropogenic meander cutoff along the Ucayali River, Peruvian Amazon, *Geogr. Rev.*, *95*(1), 122–135.

Adams, J. B., D. E. Sabol, V. Kapos, R. A. Filho, D. A. Roberts, M. O. Smith, and A. R. Gillespie (1993), Classification of multispectral images based on fractions of endmembers: Application to land-cover change in the Brazilian Amazon, *Remote Sens. Environ.*, *4257*(94), doi:10.1016/0034-4257(94)00098-8.

Allen, G. H., and T. M. Pavelsky (2015), Patterns of river width and surface area revealed by the satellite-derived North American River Width data set, *Geophys. Res. Lett.*, *42*, 395–402, doi:10.1002/2014GL062764.

Asner, G. P., W. Llactayo, R. Tupayachi, and E. R. Luna (2013), Elevated rates of gold mining in the Amazon revealed through high-resolution monitoring, *Proc. Natl. Acad. Sci. U. S. A.*, *110*(46), 18,454–18,459, doi:10.1073/pnas.1318271110.

Baki, A. B. M., and T. Y. Gan (2012), Riverbank migration and island dynamics of the braided Jamuna River of the Ganges-Brahmaputra basin using multi-temporal Landsat images, *Quat. Int.*, *263*, 148–161, doi:10.1016/j.quaint.2012.03.016.

Bazi, Y., and F. Melgani (2006), Toward an optimal SVM classification system for hyperspectral remote sensing images, *IEEE Trans. Geosci. Remote Sens.*, *44*(11), 3374–3385, doi:10.1109/TGRS.2006.880628.

Bertoldi, W., L. Zanoni, and M. Tubino (2010), Assessment of morphological changes induced by flow and flood pulses in a gravel bed braided river: The Tagliamento River (Italy), *Geomorphology*, *114*(3), 348–360, doi:10.1016/j.geomorph.2009.07.017.

Biedenharn, D. S., C. R. Thorne, and C. C. Watson (2000), Recent morphological evolution of the Lower Mississippi River, *Geomorphology*, *34*, 227–249, doi:10.1016/S0169-555X(00)00011-8.

Bradley, C., and D. G. Smith (1984), Meandering channel response to altered flow regime: Milk River, Alberta and Montana, *Water Resour. Res.*, *20*(12), 1913–1920, doi:10.1029/WR020i012p01913.

Bradley, D. N., and G. E. Tucker (2013), The storage time, age, and erosion hazard of laterally accreted sediment on the floodplain of a simulated meandering river, *J. Geophys. Res. Earth Surf.*, *118*, 1308–1319, doi:10.1002/jgrf.20083.

Butt, M. A., and P. Maragos (1998), Optimum design of chamfer distance transforms, *IEEE Trans. Image Process.*, *7*(10), 1477–1484, doi:10.1109/83.718487.

Clerici, A., and S. Perego (2016), A set of GRASS GIS-based shell scripts for the calculation and graphical display of the main morphometric parameters of a river channel, *Int. J. Geosci.*, *7*(2), 135–143, doi:10.4236/ijg.2016.72011.

Constantine, J. A., T. Dunne, J. Ahmed, C. J. Legleiter, and E. D. Lazarus (2014), Sediment supply as a driver of river meandering and floodplain evolution in the Amazon basin, *Nat. Geosci.*, *7*(12), 899–903, doi:10.1038/ngeo2282.

Coomes, O., C. Abizaid, and M. Lapointe (2009), Human modification of a large meandering Amazonian river: Genesis, ecological and economic consequences of the Masisea cutoff on the central Ucayali, Peru, *Ambio*, *38*(3), 130–134, doi:10.1579/0044-7447-38.3.130.

da Paz, A. R., W. Collischonn, A. Risso, and C. A. B. Mendes (2008), Errors in river lengths derived from raster digital elevation models, *Comput. Geosci.*, *34*, 1584–1596, doi:10.1016/j.cageo.2007.10.009.

Daniel, J. F. (1971), Channel movement of meandering Indiana streams, USGS Professional Paper 732-A.

Espinoza Villar, J. C., J. L. Guyot, J. Ronchail, G. Cochonneau, N. Filizola, P. Fraizy, D. Labat, E. de Oliveira, J. J. Ordoñez, and P. Vauchel (2009), Contrasting regional discharge evolutions in the Amazon basin (1974–2004), *J. Hydrol.*, *375*(3–4), 297–311, doi:10.1016/j.jhydrol.2009.03.004.

Ettmer, B., and C. A. Alvarado-Ancieta (2010), Morphological development of the Ucayali River, Peru without human impacts, *Waldökol. Landschaftsforsch. Naturschutz*, *10*, 77–84.

Fisher, G. B., B. Bookhagen, and C. B. Amos (2013), Channel planform geometry and slopes from freely available high-spatial resolution imagery and DEM fusion: Implications for channel width scalings, erosion proxies, and fluvial signatures in tectonically active landscapes, *Geomorphology*, *194*, 46–56, doi:10.1016/j.geomorph.2013.04.011.

Foody, G. M., and A. Mathur (2006), The use of small training sets containing mixed pixels for accurate hard image classification: Training on mixed spectral responses for classification by a SVM, *Remote Sens. Environ.*, *103*(2), 179–189, doi:10.1016/j.rse.2006.04.001.
Frias, C. E., J. D. Abad, A. Mendoza, J. Paredes, C. Ortals, and H. Montoro (2015), Planform evolution of two anabranching structures in the Upper Peruvian Amazon River, *Water Resour. Res.*, *51*, 2742–2759, doi:10.1002/2014WR015836.
Gautier, E., D. Brunstein, P. Vauchel, M. Roulet, O. Fuertes, J. Guyot, J. Darozzes, and L. Bourrel (2007), Temporal relations between meander deformation, water discharge and sediment fluxes in the floodplain of the Rio Beni (Bolivian Amazonia), *Earth Surf. Process. Landforms*, *248*, 230–248, doi:10.1002/esp.1394.
Gibbs, R. J. (1967), The geochemistry of the Amazon River system: Part I. The factors that control the salinity and the composition and concentration of the suspended solids, *Bull. Geol. Soc. Am.*, *78*(10), 1203–1232, doi:10.1130/0016-7606(1967)78[1203:TGOTAR]2.0.CO;2.
Güneralp, I., J. D. Abad, G. Zolezzi, and J. M. Hooke (2012), Advances and challenges in meandering channels research, *Geomorphology*, *163*, 1–9, doi:10.1016/j.geomorph.2012.04.011.
Gupta, N., P. M. Atkinson, and P. A. Carling (2013), Decadal length changes in the fluvial planform of the River Ganga: Bringing a mega-river to life with Landsat archives, *Remote Sens. Lett.*, *4*(1), 1–9, doi:10.1080/2150704X.2012.682658.
Handy, R. (1972), Alluvial cutoff dating from subsequent growth of a meander, *Geol. Soc. Am. Bull.*, *83*(2), 475–480, doi:10.1130/0016-7606(1972)83.
Harmar, O. P., and N. J. Clifford (2006), Planform dynamics of the Lower Mississippi River, *Earth Surf. Process. Landforms*, *31*(7), 825–843, doi:10.1002/esp.1294.
Harrelson, C., C. L. Rawlins, and J. Potyondy (1994), Stream channel reference sites: an illustrated guide to field technique, *USDA For. Serv. Gen. Tech. Rep. RM-245*, 61.
Hickin, E. J., and G. C. Nanson (1975), The character of channel migration on the Beatton River, Northeast British Columbia, Canada, *Geol. Soc. Am. Bull.*, *86*(4), 487, doi:10.1130/0016-7606(1975)86<487:TCOCMO>2.0.CO;2.
Hickin, E. J., and H. M. Sichingabula (1989), The geomorphic impact of the catastrophic October 1984 flood on the planform of Squamish River, southwestern British Columbia, *Can. J. Earth Sci.*, *26*(2), 337–337, doi:10.1139/e89-030.
Hooke, J. M. (2003), River meander behaviour and instability: A framework for analysis, *Trans. Inst. Br. Geogr.*, 238–253.
Hooke, J. M. (2004), Cutoffs galore: Occurrence and causes of multiple cutoffs on a meandering river, *Geomorphology*, *61*, 225–238, doi:10.1016/j.geomorph.2003.12.006.
Hooke, J. M. (2013), River meandering, *Treatise Geomorphol.*, *9*, 260–288, doi:10.1016/B978-0-12-374739-6.00241-4.
Hooke, J. M., and C. Redmond (1989), Use of cartographic sources for analysing river channel change with examples from Britain, in *Historical Change in Large Alluvial Rivers*, edited by G. E. Petts, H. Moller, and A. L. Roux, pp. 79–93, J. Wiley, Chichester, U. K.
Howard, A. D. (1996), Modelling channel evolution and floodplain morphology, in *Floodplain Processes*, pp. 15–62, Wiley, Chichester.
Ikeda, S., G. Parker, and K. Sawai (1981), Bend theory of river meanders. Part 1. Linear development, *J. Fluid Mech.*, *112*, 363–377, doi:10.1017/s0022112081000451.
Kalliola, R., J. Salo, M. Puhakka, and M. Rajasilta (1992), Upper Amazon channel migration, *Naturwissenschaften*, *79*, 75–79, doi:10.1007/BF01134444.
Kieler, B., W. Huang, J. Haunert, and J. Jiang (2009), Matching river datasets of different scales, *Adv. GISci.*, 135–154, doi:10.1007/978-3-642-00318-9.
Kiss, T., and V. Blanka (2012), River channel response to climate- and human-induced hydrological changes: Case study on the meandering Hernád River, Hungary, *Geomorphology*, *175–176*, 115–125, doi:10.1016/j.geomorph.2012.07.003.
Lam, L., S.-W. Lee, and C. Y. Suen (1992), Thinning methodologies—A comprehensive survey, *IEEE Trans. Pattern Anal. Mach. Intell.*, *14*(9), 869–885, doi:10.1109/34.161346.
Lane, E. W. (1947), The effect of cutting off bends in rivers., in *University of Iowa Studies in Engineering. Proceedings of the Third Hydraulics Conference*, pp. 230–240, Iowa City, Iowa.
Larsen, E. W., A. K. Fremier, and E. H. Girvetz (2006), Modeling the effects of variable annual flow on river channel meander migration patterns, Sacramento River, California, USA, *J. Am. Water Resour. Assoc.*, 1063–1075, doi:10.1111/j.1752-1688.2006.tb04514.x.
Latrubesse, E. M., J. C. Stevaux, and R. Sinha (2005), Tropical rivers, *Geomorphology*, *70*, 187–206, doi:10.1016/j.geomorph.2005.02.005.
Lauer, J. W. (2006) Channel Planform Statistics Tool (NCED Stream Restoration Toolbox).
Lauer, J. W., and G. Parker (2008), Net local removal of floodplain sediment by river meander migration, *Geomorphology*, *96*(1–2), 123–149, doi:10.1016/j.geomorph.2007.08.003.
Lavado Casimiro, W. S., D. Labat, J. Ronchail, J. C. Espinoza, and J. L. Guyot (2013), Trends in rainfall and temperature in the Peruvian Amazon-Andes basin over the last 40 years (1965–2007), *Hydrol. Process.*, *27*(20), 2944–2957, doi:10.1002/hyp.9418.
Legg, N. T., C. Heimburg, B. D. Collins, and P. L. Olson (2014), *The Channel Migration Toolbox: ArcGIS Tools for Measuring Stream*, Wash. State Dep. of Ecol., Olympia.
Lu, D., P. Mausel, M. Batistella, and E. Moran (2004), Comparison of land-cover classification methods in the Brazilian Amazon basin, *Photogramm. Eng. Remote Sens.*, *70*(6), 723–731, doi:10.14358/pers.70.6.723.
Martha, T. R., A. Sharma, and K. V. Kumar (2014), Development of meander cutoffs-a multi-temporal satellite-based observation in parts of Sindh River, Madhya Pradesh, India, *Arab. J. Geosci.*, doi:10.1007/s12517-014-1582-9.
Martinez, J. M., and T. Le (2007), Mapping of flood dynamics and spatial distribution of vegetation in the Amazon floodplain using multitemporal SAR data, *Remote Sens. Environ.*, *108*, 209–223, doi:10.1016/j.rse.2006.11.012.
Midha, N., and P. K. Mathur (2014), Channel characteristics and planform dynamics in the Indian Terai, Sharda River, *Environ. Manage.*, *53*(1), 120–34, doi:10.1007/s00267-013-0196-4.
Nagata, T., Y. Watanabe, H. Yasuda, and A. Ito (2014), Development of a meandering channel caused by the planform shape of the river bank, *Earth Surf. Dyn.*, *2*(1), 255–270, doi:10.5194/esurf-2-255-2014.
Pal, M., and P. M. Mather (2005), Support vector machines for classification in remote sensing, *Int. J. Remote Sens.*, *26*(5), 1007–1011, doi:10.1080/01431160512331314083.
Pavelsky, T. M., and L. C. Smith (2008), RivWidth: A software tool for the calculation of river widths from remotely sensed imagery, *IEEE Geosci. Remote Sens. Lett.*, *5*(1), 70–73, doi:10.1109/LGRS.2007.908305.
Perucca, E., C. Camporeale, and L. Ridolfi (2006), Influence of river meandering dynamics on riparian vegetation pattern formation, *J. Geophys. Res.*, *111*, G01001, doi:10.1029/2005JG000073.
Puhakka, M., R. Kalliola, M. Rajasilta, and J. Salo (1992), River types, site evolution and successional vegetation patterns in Peruvian Amazonia, *J. Biogeogr.*, *19*(6), 651–665, doi:10.2307/2845707.
Rhoads, B. L., Q. W. Lewis, and W. Andresen (2016), Historical changes in channel network extent and channel planform in an intensively managed landscape: Natural versus human-induced effects, *Geomorphology*, *252*, 17–31, doi:10.1016/j.geomorph.2015.04.021.

Rodnight, H., G. A. T. Duller, S. Tooth, and A. G. Wintle (2005), Optical dating of a scroll-bar sequence on the Klip River, South Africa, to derive the lateral migration rate of a meander bend, *Holocene*, *15*(6), 802–811, doi:10.1191/0959683605hl854ra.

Rowland, J. C., E. Shelef, P. A. Pope, J. Muss, C. Gangodagamage, S. P. Brumby, and C. J. Wilson (2016), A morphology independent methodology for quantifying planview river change and characteristics from remotely sensed imagery, *Remote Sens. Environ.*, *184*, 212–228, doi:10.1016/j.rse.2016.07.005.

Santini, W., et al. (2015), Sediment budget in the Ucayali River basin, an Andean tributary of the Amazon River, *Proc. Int. Assoc. Hydrol. Sci.*, *367*, 320–325, doi:10.5194/piahs-367-320-2015.

Savitzky, A., and M. J. E. Golay (1964), Smoothing and differentiation of data by simplified least squares procedures, *Anal. Chem.*, *36*(8), 1627–1639, doi:10.1021/ac60214a047.

Schwendel, A. C., A. P. Nicholas, R. Aalto, G. H. Sambrook Smith, and S. Buckley (2015), Interaction between meander dynamics and floodplain heterogeneity in a large tropical sand-bed river: The Rio Beni, Bolivian Amazon, *Earth Surf. Process. Landforms*, *40*(15), 2026–2040, doi:10.1002/esp.3777.

Schwenk, J. (2016), Meandering rivers: interpreting dynamics from planform geometry and the secret lives of migrating meanders, PhD thesis, Univeristy of Minnesota, Twin Cities.

Schwenk, J., and E. Foufoula-Georgiou (2016), Meander cutoffs nonlocally accelerate up- and downstream migration and channel widening, *Geophys. Res. Lett.*, *43*, doi:10.1002/2016GL071670.

Schwenk, J., M. Fratkin, A. Khandelwal, V. Kumar, and E. Foufoula-Georgiou (2015a), Accelerated migration due to cutoffs in the Ucayali River, paper presented at 2015 Fall Meeting, AGU, San Francisco, Calif.

Schwenk, J., S. Lanzoni, and E. Foufoula-Georgiou (2015b), The life of a meander bend: Connecting shape and dynamics via analysis of a numerical model, *J. Geophys. Res. Earth Surf.*, *120*, 690–710, doi:10.1002/2014JF003252.

Seminara, G., G. Zolezzi, M. Tubino, and D. Zardi (2001), Downstream and upstream influence in river meandering. Part 2. Planimetric development, *J. Fluid Mech.*, *438*, doi:10.1017/S0022112001004281.

Słowik, M. (2015), Is history of rivers important in restoration projects? The example of human impact on a lowland river valley (the Obra River, Poland), *Geomorphology*, *251*, 50–63, doi:10.1016/j.geomorph.2015.05.031.

Smith, L. C., B. L. Isacks, A. L. Bloom, and A. B. Murray (1996), Estimation of discharge from three braided rivers using synthetic aperture radar satellite imagery: Potential application to ungaged basins, *Water Resour. Res.*, *32*(7), 2021–2034, doi:10.1029/96WR00752.

Stolum, H.-H. (1998), Planform geometry and dynamics of meandering rivers, *Geol. Soc. Am. Bull.*, *110*(11), 1485–1498, doi:10.1130/0016-7606(1998)110<1485:PGADOM>2.3.CO;2.

Sun, T., P. Meakin, T. Jøssang, and K. Schwarz (1996), A simulation model for meandering rivers, *Water Resour. Res.*, *32*(9), 2937–2954, doi:10.1029/96WR00998.

Webster, K., J. P. Arroyo-Mora, O. T. Coomes, Y. Takasaki, and C. Abizaid (2016), A cost path and network analysis methodology to calculate distances along a complex river network in the Peruvian Amazon, *Appl. Geogr.*, *73*, 13–25, doi:10.1016/j.apgeog.2016.05.008.

Williams, G. P. (1978), Bank-full discharge of rivers, *Water Resour. Res.*, *14*(6), 1141–1154, doi:10.1029/WR014i006p01141.

Xu, D., Y. Bai, J. Ma, and Y. Tan (2011), Numerical investigation of long-term planform dynamics and stability of river meandering on fluvial floodplains, *Geomorphology*, *132*(3–4), 195–207, doi:10.1016/j.geomorph.2011.05.009.

Yang, X., M. C. Damen, and R. A. van Zuidam (1999), Satellite remote sensing and GIS for the analysis of channel migration changes in the active Yellow River Delta, China, *Int. J. Appl. Earth Obs. Geoinf.*, *1*(2), 146–157, doi:10.1016/S0303-2434(99)85007-7.

Yao, Z., J. Xiao, W. Ta, and X. Jia (2012), Planform channel dynamics along the Ningxia-Inner Mongolia reaches of the Yellow River from 1958 to 2008: Analysis using Landsat images and topographic maps, *Environ. Earth Sci.*, *70*(1), 97–106, doi:10.1007/s12665-012-2106-0.

Zinger, J. A., B. L. Rhoads, and J. L. Best (2011), Extreme sediment pulses generated by bend cutoffs along a large meandering river, *Nat. Geosci.*, *4*(10), 675–678, doi:10.1038/ngeo1260.